Cellular/Molecular

$\alpha_2\delta2$ Controls the Function and Trans-Synaptic Coupling of $Ca_v1.3$ Channels in Mouse Inner Hair Cells and Is Essential for Normal Hearing

Barbara Fell,[1] Stephanie Eckrich,[1] Kerstin Blum,[1] Tobias Eckrich,[1] Dietmar Hecker,[2] Gerald J. Obermair,[4] Stefan Münkner,[1] Veit Flockerzi,[3] Bernhard Schick,[2] and Jutta Engel[1]

[1]Department of Biophysics, Center for Integrative Physiology and Molecular Medicine (CIPMM), and Departments of [2]Otorhinolaryngology and [3]Experimental and Clinical Pharmacology and Toxicology, School of Medicine, Saarland University, 66421 Homburg, Germany, and [4]Medical University Innsbruck, Division of Physiology, 6020 Innsbruck, Austria

The auxiliary subunit $\alpha_2\delta2$ modulates the abundance and function of voltage-gated calcium channels. Here we show that $\alpha_2\delta2$ mRNA is expressed in neonatal and mature hair cells. A functional $\alpha_2\delta2$-null mouse, the ducky mouse (du), showed elevated auditory brainstem response click and frequency-dependent hearing thresholds. Otoacoustic emissions were not impaired pointing to normal outer hair cell function. Peak Ca^{2+} and Ba^{2+} currents of mature du/du inner hair cells (IHCs) were reduced by 30–40%, respectively, and gating properties, such as the voltage of half-maximum activation and voltage sensitivity, were altered, indicating that $Ca_v1.3$ channels normally coassemble with $\alpha_2\delta2$ at IHC presynapses. The reduction of depolarization-evoked exocytosis in du/du IHCs reflected their reduced Ca^{2+} currents. Ca^{2+}- and voltage-dependent K^+ (BK) currents and the expression of the pore-forming BKα protein were normal. $Ca_v1.3$ and $Ca_v\beta2$ protein expression was unchanged in du/du IHCs, forming clusters at presynaptic ribbons. However, the close apposition of presynaptic $Ca_v1.3$ clusters with postsynaptic glutamate receptor GluA4 and PSD-95 clusters was significantly impaired in du/du mice. This implies that, in addition to controlling the expression and gating properties of $Ca_v1.3$ channels, the largely extracellularly localized $\alpha_2\delta2$ subunit moreover plays a so far unknown role in mediating trans-synaptic alignment of presynaptic Ca^{2+} channels and postsynaptic AMPA receptors.

Key words: AMPA receptor; *Cacna2d2*; GluA4; inner hair cell; PSD-95; ribbon synapse

Significance Statement

Inner hair cells possess calcium channels that are essential for transmitting sound information into synaptic transmitter release. Voltage-gated calcium channels can coassemble with auxiliary subunit $\alpha_2\delta$ isoforms 1–4. We found that hair cells of the mouse express the auxiliary subunit $\alpha_2\delta2$, which is needed for normal hearing thresholds. Using a mouse model with a mutant, nonfunctional $\alpha_2\delta2$ protein, we showed that the $\alpha_2\delta2$ protein is necessary for normal calcium currents and exocytosis in inner hair cells. Unexpectedly, the $\alpha_2\delta2$ protein is moreover required for the optimal spatial alignment of presynaptic calcium channels and postsynaptic glutamate receptor proteins across the synaptic cleft. This suggests that $\alpha_2\delta2$ plays a novel role in organizing the synapse.

Introduction

Voltage-gated calcium channels (VGCCs) are protein complexes composed of a main, pore-forming α_1 subunit and auxiliary $\alpha_2\delta$ and β subunits. The traditional view is that auxiliary subunits modulate biophysical properties of VGCCs, which are mostly determined by the α_1 subunit, and assist in the trafficking and proper surface expression of the channel complex (Catterall, 2000; Dolphin, 2012a, 2013). Recent evidence suggests an addi-

Received Aug. 18, 2014; revised Sept. 1, 2016; accepted Sept. 3, 2016.

Author contributions: B.F., S.E., G.J.O., B.S., and J.E. designed research; B.F., S.E., K.B., T.E., D.H., and G.J.O. performed research; S.M. and V.F. contributed unpublished reagents/analytic tools; B.F., S.E., K.B., T.E., D.H., G.J.O., S.M., B.S., and J.E. analyzed data; B.F., S.E., K.B., D.H., G.J.O., V.F., and J.E. wrote the paper.

This work was supported by Deutsche Forschungsgemeinschaft (DFG) Sonderforschungsbereich (SFB) 894 (Grants A8 to J.E. and A3 to V.F.), DFG SFB 1027 (Grant A4 to J.E.), the Austrian Science Fund (Grants P24079 and SFB F4415), and Saarland University. We thank Jennifer Ihl, Angela Di Turi, Roman Egger, and Stefanie Geisler for excellent technical assistance; and Yvonne Schwarz for help with data analysis.

The authors declare no competing financial interests.

Correspondence should be addressed to Dr. Jutta Engel, Department of Biophysics, Center for Integrative Physiology and Molecular Medicine (CIPMM), Saarland University, School of Medicine, Building 48, 66421 Homburg, Germany. E-mail: jutta.engel@uni-saarland.de.

DOI:10.1523/JNEUROSCI.3468-14.2016

 0270-6474/16/3611024-13$15.00/0

tional role of $\alpha_2\delta$ subunits in synaptogenesis (Eroglu et al., 2009; Kurshan et al., 2009; Dolphin, 2012a; Geisler et al., 2015) and for synaptic morphology (Pirone et al., 2014). $\alpha_2\delta$ subunits, encoded by one of the four genes *CACNA2D1–4*, consist of a large extracellular glycosylated α_2 peptide linked to a small membrane-anchored δ peptide (Davies et al., 2007; Dolphin, 2012a, 2013). Coexpressing any of the isoforms $\alpha_2\delta1$–3 with various α_1 and β subunits results in functional channels with increased current amplitudes and altered channel gating (Davies et al., 2007; Dolphin, 2012a, 2013). In the brain, the isoforms $\alpha_2\delta1$, $\alpha_2\delta2$, and $\alpha_2\delta3$ are widely expressed (Cole et al., 2005; Schlick et al., 2010), whereas $\alpha_2\delta4$ is mainly found in the retina (De Sevilla Müller et al., 2013; Knoflach et al., 2013). Genetic deletion of $\alpha_2\delta1$ or $\alpha_2\delta3$ yielded relatively mild phenotypes (Fuller-Bicer et al., 2009; Neely et al., 2010; Pirone et al., 2014). In contrast, the "ducky" (du) mutation of *Cacna2d2* encoding $\alpha_2\delta2$ results in a functional $\alpha_2\delta2$-null mouse (du/du mouse) with a severe phenotype, including cerebellar ataxia, epilepsy, reduced body weight, and premature death (Barclay et al., 2001; Brodbeck et al., 2002). Cerebellar Purkinje cells of ducky mice exhibit 35% smaller whole-cell Ca^{2+} currents mediated by P-type ($Ca_v2.1$) Ca^{2+} channels and abnormal morphology of their dendritic trees (Barclay et al., 2001; Brodbeck et al., 2002). The ducky mutation is a genomic rearrangement involving the *Cacna2d2* gene, which is disrupted after exon 3 (of 39 exons; Barclay et al., 2001). A short truncated protein is still produced but not targeted correctly (Brodbeck et al., 2002). The characterization of other $\alpha_2\delta2$-deficient mouse models revealed phenotypes very similar to that of du/du mice (Brill et al., 2004; Ivanov et al., 2004; Donato et al., 2006), altogether indicating that $\alpha_2\delta2$ is indispensable for the Ca^{2+} channel complex consisting of $Ca_v2.1$ and $Ca_v\beta4$ at inhibitory Purkinje cell presynapses. Recently in humans, a missense and a nonsense mutation in *CACNA2D2* were identified, both of which cause early infantile epileptic encephalopathy with severe developmental impairment and intellectual disability (Edvardson et al., 2013; Pippucci et al., 2013).

Inner hair cells (IHCs) transform sound-evoked depolarization into graded release of the transmitter glutamate. They express voltage-gated Ca^{2+} channels, which almost exclusively consist of the L-type $Ca_v1.3$ subunit (Platzer et al., 2000; Brandt et al., 2003; Dou et al., 2004) and are localized predominantly in clusters underneath the synaptic ribbons (Vincent et al., 2014; Wong et al., 2014). The $Ca_v1.3$ subunits of IHCs predominantly coassemble with the β subunit $Ca_v\beta2$ (Neef et al., 2009), with some contribution of $Ca_v\beta3$ and $Ca_v\beta4$ (Kuhn et al., 2009). The nature of the third partner of the Ca^{2+} channel complex, the $\alpha_2\delta$ subunit, was unknown so far.

Materials and Methods

Animals. Mice carrying a mutation of the *Cacna2d2* gene coding for $\alpha_2\delta2$ with genomic rearrangement (*Cacna2d2*^{du} or ducky allele; Barclay et al., 2001) were obtained from the The Jackson Laboratory (http://jaxmice.jax.org/strain/012889.html). They were backcrossed into C57BL/6N (obtained from Charles River) for five or more generations. Cochleae were dissected after mice had been killed by decapitation with isoflurane anesthesia or after cervical dislocation for exocytosis experiments. Animals were housed with free access to food and water at an average temperature of 22°C and a 12 h light/dark cycle. All experiments were performed in accordance with the European Communities Council Directive (86/609/EEC) and approved by regional board for scientific animal experiments of the Saarland, Germany. Genotyping of du/du mice was adapted from Brodbeck et al. (2002). Mice of either sex were used. Hearing measurements and all electrophysiological recordings were performed on du/du mice and wild-type (wt) littermates. For immunofluorescence experiments, mostly wt mice, but in some cases heterozygous (du/wt) littermates, were used as control (ctrl) animals. Heterozygous animals have a normal life expectancy and do not show any of the phenotypes of homozygous du/du mice (Barclay et al., 2001).

Quantitative real-time PCR. For quantitative PCR (qPCR) analysis, IHCs and outer hair cells (OHCs) from postnatal day 6 (P6) or P20–P25 mice were selectively harvested with micropipettes under microscope control as described previously (Baig et al., 2011). For reverse transcription (RT), 9 μl of cell lysate was mixed with 2 μl of random primers $pd(N)_6$ (50 μM; Applied Biosystems) and 1 μl of dNTP (deoxynucleotidetriphosphate) mix (10 mM; New England Biolabs), incubated at 65°C for 5 min and stored on ice for 1 min. An RT mix (8 μl; Life Technologies) consisting of 5× reverse transcription buffer, 0.1 M dithiothreitol, 2 U/μl RNAseOUT and 2.5 U/μl reverse transcriptase Superscript III was added, and each tube was incubated at 50°C for 150 min followed by 70°C for 30 min. cDNA was stored at −20°C. The abundance of different $\alpha_2\delta$ subunit transcripts in IHC and OHC cDNA was assessed by TaqMan qPCR using a standard curve method, as previously described (Schlick et al., 2010). cDNA of pooled hair cells (30–630) was split into 12 samples to simultaneously run qPCR-TaqMan assays for all $\alpha_2\delta$ subunit genes and the endogenous control gene *Hprt1* in duplicate. TaqMan gene expression assays specific for the four $\alpha_2\delta$ isoforms were designed to span exon–exon boundaries and were purchased from Applied Biosystems. The following assays were used [identified as name (gene symbol), assay ID; Applied Biosystems]: $\alpha_2\delta1$ (*Cacna2d1*), Mm00486607_m1; $\alpha_2\delta2$ (*Cacna2d2*), Mm00457825_m1; $\alpha_2\delta3$ (*Cacna2d3*), Mm00486613_m1; and $\alpha_2\delta4$ (*Cacna2d4*), Mm01190105_m1. The expression of hypoxanthine phosphoribosyl-transferase 1 (*Hprt1*; Mm00446968_m1) was used as the endogenous control. The qPCR (50 cycles) was performed in duplicate using total cDNA (see above) and the specific TaqMan gene expression assay for each 20 μl reaction in TaqMan Universal PCR Master Mix (Applied Biosystems). Samples without cDNA were used as controls. Analyses were performed using the 7500 Fast System (Applied Biosystems). The C_t values for each gene expression assay were recorded for each individual preparation and the molecule numbers were calculated for each $\alpha_2\delta$ subunit from their respective standard curve (Schlick et al., 2010). Expression of *Hprt1* was used to evaluate the total mRNA abundance and to allow a direct comparison between the expression levels in different preparations.

Hearing measurements. Auditory brainstem response (ABR) and distortion product otoacoustic emissions (DPOAEs) were recorded in anesthetized mice aged 3–4 weeks as described previously (Rüttiger et al., 2004; Engel et al., 2006). For anesthesia, a mixture of ketamine-hydrochloride [75 mg/kg body weight (b.w.); Ketavet 100, Pharmacia] and xylazine-hydrochloride (5 mg/kg b.w.; Rompun 290, Bayer) was injected intraperitoneally with an injection volume of 5 ml/kg b.w. Anesthesia was maintained by subcutaneous application of one-third of the initial dose, typically in 30 min intervals. Body temperature was maintained with a temperature-controlled heating pad. ABR thresholds were determined with click (100 μs) and pure tone stimuli (3 ms plus 1 ms rise/fall time, 2–45 kHz) with electrodes placed at the ear (positive) and vertex (reference). ABR waveforms for click stimuli were determined 40 dB above threshold for each individual animal. Cubic $2 \cdot f1 - f2$ (where f is frequency) DPOAE amplitudes for the two stimulus primaries with frequencies f1 and f2, and $f2 = 1.2 \cdot f1$, and sound pressure level L1 = 55 dB SPL and L2 = 45 dB SPL for the first and the second primary, respectively, were measured at either 16 kHz as well as in the range between 10 and 18 kHz using 0.5 kHz steps followed by averaging (Schimmang et al., 2003; Hecker et al., 2011). Latencies and peak-to-peak amplitudes of the ABR waveforms were extracted from each individual waveform. Click ABR thresholds, wave I latencies of ABR waveforms, and DPOAE amplitudes were analyzed using the Mann–Whitney *U* test; and frequency-dependent ABR thresholds were analyzed with a two-way ANOVA with Bonferroni *post hoc* test.

Electrophysiological recordings. Acutely dissected organs of Corti of 3-week-old mice were used to record Ca^{2+}/Ba^{2+} and K^+ currents. The bath solution for Ca^{2+} and K^+ currents (B1) contained the following (in mM): 70 lactobionate·NaOH, 83 NaCl, 10 HEPES, 5.8 KCl, 5.6 glucose, 1.3 $CaCl_2$, 0.95 $MgCl_2$, and 0.7 NaH_2PO_4. The bath solution for Ba^{2+}

currents (B2) contained the following: 72 lactobionate•NaOH, 40 NaCl, 35 TEA, 15 4-AP, 10 $BaCl_2$, 10 HEPES, 5.6 KCl, 5.3 glucose, and 1 $MgCl_2$. Both solutions were adjusted to pH 7.35 and 320 mosmol/kg. For Ca^{2+} current recordings, the specimen was locally superfused with B3 (in mM), as follows: 72.5 lactobionate•NaOH, 40 NaCl, 35 TEA, 15 4-AP, 10 $CaCl_2$, 10 HEPES, 5.6 KCl, 5.6 glucose, 0.9 $MgCl_2$, 0.1 linopirdine, and 0.0005 apamin, pH 7.35 and 320 mosmol/kg. The pipette solution for Ca^{2+}/Ba^{2+} currents contained the following (in mM): 110 Cs^+ methane sulfonate, 20 CsCl, 10 Na^+ phosphocreatine, 5 HEPES, 5 EGTA, 4 $MgCl_2$, 4 Na_2ATP, 0.3 GTP, 0.1 $CaCl_2$; for exocytosis measurements EGTA concentration was 1 mM. The pipette solution for K^+ currents consisted of the following (in mM): 110 K^+ gluconate, 20 KCl, 10 Na^+ phosphocreatine, 5 HEPES, 5 EGTA, 4 $MgCl_2$, 4 Na_2ATP, 0.1 GTP, and 0.1 $CaCl_2$; and all pipette solutions were adjusted to pH 7.35 and 305 mosmol/kg.

Uncompensated series resistance was corrected by 70–80% for K^+ current and membrane capacitance recordings. Linear leak subtraction was performed off-line, and voltages were corrected by subtracting liquid junction potentials (LJPs) of 6 mV (Ca^{2+} currents), 8 mV (Ba^{2+} currents), and 10 mV (K^+ currents). *I–V* curves of Ca^{2+}/Ba^{2+} currents were fitted to a second-order Boltzmann function times Goldman–Hodgkin–Katz driving force to determine parameters of the activation curve, the voltage of half-maximum activation, V_h, and the voltage sensitivity of activation, the slope factor k, according to the following equation:

$$I = -P_{\max} z f v \left(\frac{[Ca]_o}{e^{\nu-1}} + \frac{[Ca]_i}{e^{-(\nu+1)}} \right) \cdot \left(\frac{1}{1+e^{\frac{(V_h-V)}{k}}} \right)^2, \quad (1)$$

where I is the current at the time the *I–V* was calculated (averaged over 7–8 ms after depolarization), $P_{\max}$ is the maximum permeability, and $\nu = zFV/(RT)$, with z being 2, F the Faraday constant, R the universal gas constant, T the absolute temperature, and V the membrane potential. $[Ca]_i$ (set at 50 nM) and $[Ca]_o$ denote the intracellular and extracellular Ca^{2+} concentrations, respectively. Fits for Ba^{2+} as charge carrier were performed accordingly.

The degree of I_{Ca}/I_{Ba} inactivation 300 ms after peak was determined as follows:

$$\%\text{inactivation} = \left(1 - \frac{I_{\text{test}}}{I_{\text{peak}}}\right) \cdot 100(\%), \quad (2)$$

where I_{peak} is the maximum of the peak current trace at $t = t_{\text{peak}}$, and I_{test} is the current determined at $t = t_{\text{peak}} + 300$ ms. The inactivation time course of I_{Ca}/I_{Ba} in the 300 ms following the peak was fitted with a monoexponential function, as follows:

$$I(t) = A_0 + A_1 e^{-\frac{t}{\tau}}, \quad (3)$$

with A_0 and A_1 being constants, and τ the time constant of inactivation.

I–V curves of K^+ currents were fitted to a first-order Boltzmann function times driving force according to Nernst's equation:

$$I = G_{\max} \frac{(V - V_{\text{rev}})}{1 + e^{\frac{V_h - V}{k}}}, \quad (4)$$

where V_{rev} is the reversal potential for K^+ (−73 mV), and $G_{\max}$ is the maximum conductance of the IHC K^+ currents (Kros and Crawford, 1990). Activation time constants of I_K over 700 μs after start of the depolarization were determined as follows:

$$I(t) = I_{\max}(1 - e^{-\frac{t}{\tau}}), \quad (5)$$

where $I(t)$ is the current at time t, $I_{\max}$ is the steady-state current, and τ is the time constant of activation (Marcotti et al., 2003).

Parameters of Ca^{2+}, Ba^{2+}, and K^+ currents were statistically analyzed using the Mann–Whitney *U* test. *I–V* curves were analyzed with a two-way ANOVA with Bonferroni *post hoc* test.

Exocytosis measurements. Voltage-evoked capacitance changes were recorded from IHCs of P18–P20 mice. The bath was perfused with B1; IHCs were locally superfused with B4 as follows (in mM): 72.5 lactobionate•NaOH, 40 NaCl, 35 TEA, 15 4-AP, 5 $CaCl_2$, 10 HEPES, 5.6 KCl, 5.6 glucose, 1 $MgCl_2$, and 0.1 linopirdine, at pH 7.35 and 320 mosmol/kg. An LJP of 5 mV between the bath and pipette solution was subtracted; the small LJP change due to superfusion of B4 was neglected. Membrane capacitance measurements were performed using an Optopatch amplifier (Cairn Research Ltd) at room temperature, as described previously (Brandt et al., 2007). IHCs were depolarized for 100 ms from V_h (−85 mV) up to 45 mV in 10 mV increments. The change in membrane capacitance (ΔC_m) was calculated as the capacitance averaged over 300 ms after the voltage step (after a delay of 150 ms from the end of the step) minus the capacitance averaged over 300 ms before onset of the voltage step. For statistics of the capacitance–voltage (*C–V*) curve, a two-way ANOVA with Bonferroni *post hoc* test was used. To assess the Ca^{2+} efficiency of exocytosis, Q_{Ca} was calculated by integrating the absolute value of I_{Ca} over the time of depolarization plus tail currents for voltages less than or equal to $V_{\max}$. Fits to the individual ΔC_m–Q_{Ca} curves were made according to the following:

$$\Delta C_m = y_0 + cQ_{Ca}^N, \quad (6)$$

where y_0 is the offset and c is a scaling factor, which yielded the power N for each cell and were analyzed using Student's *t* test. Data are reported as the mean ± SEM.

Immunohistochemistry. Immunolabeling was performed on whole-mounts of the organ of Corti of 3-week-old mice. The scalae of each cochlea were injected with either 2% PFA in 100 mM PBS (Pirone et al., 2014), Zamboni's fixative (Stefanini et al., 1967), or −20°C cold ethanol and immersed in the fixative for 10–20 min on ice. After replacing the fixative with PBS, the cochlear spiral was dissected into an apical part of up to 22% of the length of the basilar membrane, corresponding to 2–8 kHz, which was designated as an apical turn, and a medial part of 22% to 45% (sometimes 60%) of the length of the basilar membrane, covering a region from 9 to 17 kHz (sometimes 26 kHz), which was designated as the medial turn. Specimens were labeled with antibodies against $Ca_v1.3$ (rabbit polyclonal, 1:500; Alomone Labs), $Ca_v\beta2$ (rabbit polyclonal, custom-made; 1:500), CtPB2/Ribeye (mouse monoclonal, 1:100; BD Transduction Laboratories), PSD-95 (mouse monoclonal, 1:1000; NeuroMab), BKα (rabbit polyclonal, 1:500; Alomone Labs; mouse monoclonal, 1:50; Antibodies-Online), SK2 (rabbit polyclonal, 1:200; Sigma-Aldrich), glutamate receptor 4/GRIA4 (goat polyclonal, 1:500; Biorbyt, which required ethanol fixation), and Acti-stain 670 Fluorescent Phalloidin (200 nM; Cytoskeleton, Inc.). Primary antibodies were detected with Cy3-conjugated (1:1500; Jackson ImmunoResearch) or Alexa Fluor 488-conjugated secondary antibodies (1:500; Invitrogen). For all immunolabeling experiments, at least three specimens of three or more animals were analyzed. *z*-stacks of fluorescence images were acquired using a confocal laser scanning microscope (model LSM700 or LSM710, Carl Zeiss Microscopy). Images (70 × 70 nm^2 pixel size) were obtained using a 63× oil objective (Planapochromat, Zeiss), 1.4 numerical aperture, with a pinhole of 1 airy unit. Stacks of 0.32-μm-thick optical slices, maximum intensity projections (MIPs) and single images were analyzed with Fiji software (Schindelin et al., 2012).

For quantifying the overlap of $Ca_v1.3$ with PSD-95 clusters, a line scan analysis was used on MIPs of double-labeled images each containing four adjacent IHCs. Ten lines measuring 10 × 0.7 μm^2 were placed on each MIP image, thereby covering ~90% of all clusters, without covering clusters twice. Corresponding pixel intensity profiles, for which a threshold of 500 was applied, yielded overlapping and single peaks of the two color channels. For analysis of cluster sizes, the channel of interest of an MIP image was subjected to background subtraction, and a thresholded binary image was created. The cluster area was analyzed automatically with Fiji (Schindelin et al., 2012). For quantification of the overlap of $Ca_v1.3$ clusters with GluA4 spots, images of 67.5 × 38.9 μm^2 size covering eight IHCs were acquired at equal laser and gain settings, and MIPs were calculated. The channel of interest of an MIP image was background subtracted. A thresholded binary image was created (0 below threshold; 1 above threshold) with thresholds of 10% of the maximum intensity of the green color channel (GluA4) and 15% of the red color channel ($Ca_v1.3$).

Table 1. Transcript numbers of $\alpha_2\delta$ subunits in samples of pooled IHCs and OHCs of the apical turn in mice before (P6) and after (P20–P25) hearing onset determined by quantitative RT-PCR

	$\alpha_2\delta1$	$\alpha_2\delta2$	$\alpha_2\delta3$	$\alpha_2\delta4$
IHCs				
P6 (40 IHCs)	1	14	3	0
P6 (120 IHCs)	3	122	23	0
P20–P25				
Mean ± SEM of eight samples with 30–170 IHCs each	0	7.4 ± 1.6	0	0
Range		1–13		
Outer hair cells				
P6 (240 OHCs)	6	30	3	5
P20–P25				
Mean ± SEM of six samples with 120–630 OHCs each	0	10.0 ± 2.3	0	0
Range		6–21		

For details, see Materials and Methods and Results.

After discarding GluA4 clusters <0.15 μm^2 and $Ca_v1.3$ clusters <0.05 μm^2, the GluA4-thresholded binary image was used as a mask for the $Ca_v1.3$-thresholded binary image to yield overlapping clusters, which were analyzed using the particle count routine in Fiji. Parameters of overlapping/segregated $Ca_v1.3$, PSD-95, and GluA4 clusters were statistically analyzed using the Mann–Whitney *U* test.

Results

Expression of $\alpha_2\delta$ mRNA in IHCs

To assess the contribution of $\alpha_2\delta$ subunits to Ca^{2+} channel complexes of hair cells, quantitative real-time PCR for $\alpha_2\delta1$–4 was performed, and transcript numbers for all $\alpha_2\delta$ subunits were obtained from standard curves, as previously established (Schlick et al., 2010). IHCs and OHCs were selectively harvested with micropipettes under microscope control, and cDNA was synthetized from mRNA by reverse transcription. At P6, transcripts for $\alpha_2\delta2$ and $\alpha_2\delta3$ were reliably detected, with $\alpha_2\delta2$ showing the highest transcript numbers (Table 1). In eight independent IHC samples of the mature cochlea (P20–P25), only $\alpha_2\delta2$ transcripts could be detected at low numbers. The same was true for OHCs at both P6 and P20–P25. $\alpha_2\delta$ transcript numbers were very low in mature hair cells, even when several hundred hair cells were pooled (Table 1), probably because of low $Ca_v1.3/\alpha_2\delta$ expression levels (Knirsch et al., 2007) and the limited number of cells. Despite the low number of detected $\alpha_2\delta2$ transcripts (1–122; Table 1) the log-transformed transcript numbers strongly and highly significantly correlated indirectly with the C_t values of the endogenous control gene Hprt1 (Pearson correlation: $r_{(17)} = -0.79$, $p < 0.001$; mean ± SEM C_t value, 33.42 ± 0.40; range, 31.36–36.94). This shows that the number of detected $\alpha_2\delta2$ transcripts reliably increased with the quantity of cDNA, while transcripts of the other $\alpha_2\delta$ isoforms were either very low (at P6) or not detectable (P20–P25). Due to the fact that reliable antibodies against $\alpha_2\delta3$ and $\alpha_2\delta2$ are not available (Dolphin, 2013), the expression of $\alpha_2\delta$ subunits in hair cells could not be tested at the protein level. Nevertheless, our qPCR revealed the consistent presence of $\alpha_2\delta2$ transcripts in hair cells before and after hearing onset, and thus we set out to study hearing and the cellular and molecular phenotypes of a functional $\alpha_2\delta2$-null mouse, the ducky mouse.

Impaired auditory function in du/du mice

Next, we assessed hearing performance of $\alpha_2\delta2$ (du/du) mutants (Fig. 1). Click ABR thresholds of du/du mice were significantly elevated (33.0 ± 12.9 dB SPL; $n = 8/15$ animals/ears) compared with wt mice (14.7 ± 2.9 dB SPL; $n = 8/16$ animals/ears; Mann–Whitney *U* test, $p < 0.001$; Fig. 1*A*, left). Average frequency-specific ABR thresholds were always larger for du/du mice than for wt mice between 2 and 45 kHz. This difference was significant in the best hearing range of mice, specifically at 11.3, 16, and 22.3 kHz (two-way ANOVA, $p < 0.01$; Fig. 1*A*). Hearing function was further tested by measuring DPOAEs, an objective indicator of the cochlear amplifier including the electromotility of OHCs. Unexpectedly, 2f1-f2 DPOAE maximum amplitudes for f2 averaged over 10–18 kHz in 0.5 kHz steps were significantly larger in du/du mice (Fig. 1*B*; wt mice: 21.9 ± 4.0 dB SPL, $n = 3/6$ animals/ears; du/du mice: 28.9 ± 3.0 dB SPL, $n = 4/8$ animals/ears; $p < 0.01$, Mann–Whitney *U* test). This suggests that OHC function was not corrupted by the lack of $\alpha_2\delta2$ and raises the question of why DPOAE amplitudes were not reduced but were even larger despite increased ABR thresholds in du/du mice. Averaged ABR waveforms for click stimuli 40 dB above threshold revealed differences between the genotypes (Fig. 1*C*). Notably, wave I, the negative peak of which appears at 1.4–1.9 ms after the start of the click stimulus in wt mice and represents the discharge of auditory nerve fibers (but see Pirone et al., 2014), was delayed by 0.3 ms ($p < 0.01$) in du/du mice. The peak-to-peak amplitude of wave I showed a tendency toward reduced values, but, due to the high variability especially in du/du mice, this reduction was not significant. Interestingly, wave III was completely distorted, suggesting that du/du mice also exhibit a central auditory processing phenotype.

Because OHCs of the apical cochlear turn of $Ca_v1.3$-deficient mice undergo early degeneration (Platzer et al., 2000), we tested for morphological integrity of OHCs in whole-mount preparations of 3-week-old mice. Apical and medial cochlear turns stained for actin with fluorescent phalloidin showed normal expression of three rows of OHCs (arrows) and normal hair bundle morphology in du/du mice compared with wt mice (Fig. 1*D*,*E*, shown for apical turns). To test whether medial efferent fibers from the brainstem, which can inhibit OHC electromotility at low to medium sound pressure levels, project normally to du/du OHCs, we labeled for the inhibitory effector K^+ channels SK2 and BK (Dulon et al., 1998; Oliver et al., 2000; Rüttiger et al., 2004). The location of apical and medial turn OHCs in mouse cochlear whole mounts and their corresponding frequencies (Müller et al., 2005; Engel et al., 2006) are illustrated in Figure 1*F*. In both du/du and wt mice, BK channels colocalized with SK2 channels in two to six patches in all three rows at the base of the OHCs, showing normal expression of the effector channels of efferent inhibitory terminals in du/du mice (Fig. 1*G*, shown for medial turns).

Ca^{2+} and Ba^{2+} currents are reduced and altered in mature IHCs of du/du mice

Increased hearing thresholds without a reduction of DPOAEs pointed to a defect of IHCs. Therefore, whole-cell Ca^{2+} and Ba^{2+} currents were recorded in 3-week-old du/du and wt apical turn IHCs. Selected current traces in response to 8 ms step depolarizations for the voltages indicated, with 10 mM Ca^{2+} as a charge carrier are shown for a typical wt IHC (Fig. 2*A*) and a typical du/du IHC (Fig. 2*B*). The peak Ca^{2+} current (I_{Ca}) was larger in the wt IHC compared with the du/du IHC. *I–V* curves averaged for 20 wt and 12 du/du IHCs showed a shift toward positive voltages and a reduction in I_{Ca} in du/du IHCs (Fig. 2*C*). Average I_{Ca} amplitudes, cell capacitance, current density, and biophysical parameters of I_{Ca} activation, such as V_h and slope factor of the Boltzmann function obtained from fits to the individual *I–V* curves (see Materials and Methods), are given in Table 2. IHCs of

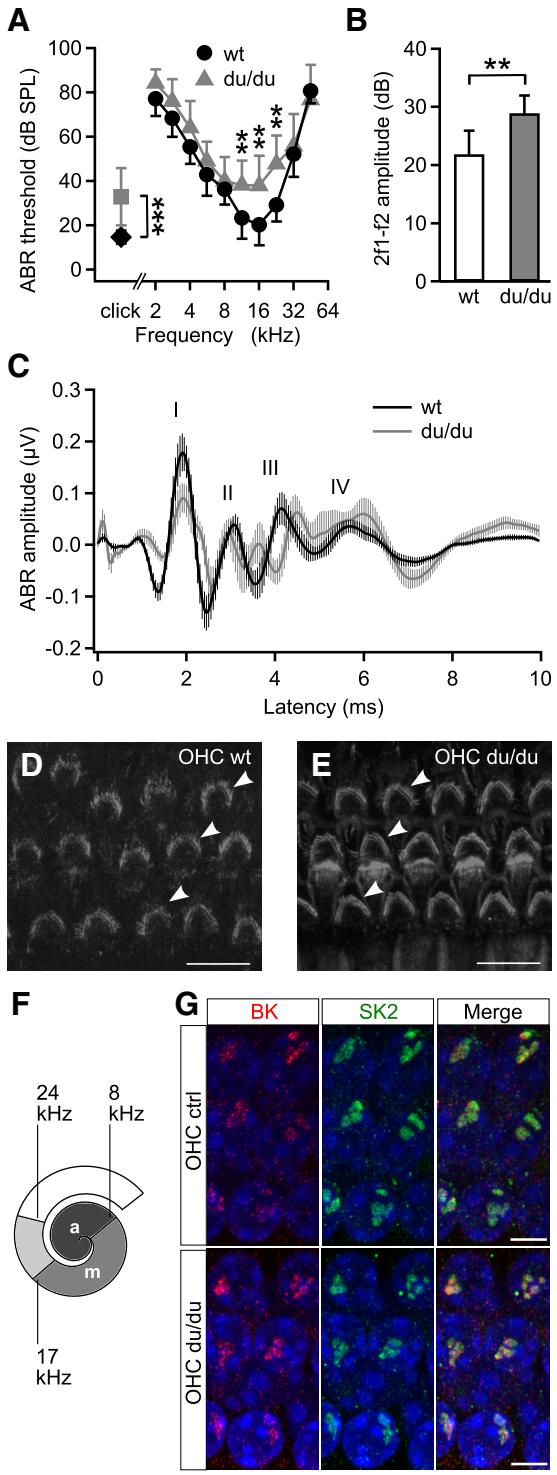

Figure 1. Hearing function and integrity of OHCs of ducky mice. ***A***, ABR thresholds (mean ± SD) of du/du mice were significantly increased for click stimuli (leftmost values: wt, $n = 8/16$ animals/ears; du/du, $n = 8/15$ animals/ears, $^{***}p < 0.001$, Mann–Whitney *U* test) and as a function of stimulus tone frequency (wt, $n = 8/16$ animals/ears; du/du, $n = 7/14$ animals/ears; $^{**}p < 0.01$, two-way ANOVA with Bonferroni *post hoc* test, effect of genotype at 11.3, 16, and 22.3 kHz). ***B***, Mean DPOAE maximum amplitudes ± SD with f1 starting at 9.1 kHz, L1 = 55 dB SPL, f2 = 1.2 • f1 averaged over 10–18 kHz, and L2 = 45 dB SPL were larger in du/du ($n = 4/8$ animals/ears) compared with wt ($n = 3/6$ animals/ears, $^{**}p < 0.01$, Mann–Whitney U test). ***C***, Averaged ABR waveforms to click stimuli at 40 dB above threshold (mean ± SEM) for 8 of 16 wt animals/ears (black) and 7 of 14 du/du animals/ears (gray). ***D***, ***E***, Normal number of OHC rows (arrowheads) and normal OHC hair bundle morphology as revealed by phalloidin staining of the apical turn of wt (***D***) and du/du (***E***) cochleae. ***F***, Sketch of a mouse cochlear whole-mount that illustrates the position of the apical turn representing 2–8 kHz and the medial turn representing 8–17 kHz, which were used in immunolabeling and electrophysiological experiments. The medial part partially reached frequencies up to 24 kHz. ***G***, Immunolabeling for the basolateral K^+ channels BK (left column) and SK2 (middle column; merged BK and SK2 immunolabeling in the right column) at the base of du/du OHCs of all three rows of the medial cochlear turn (bottom row) did not differ from that of the wt OHCs (top row). This indicates the normal expression of OHC K^+ channels that mediate inhibition by medial olivocochlear fibers.

du/du mice showed a highly significant reduction of peak I_{Ca} of 37.2% and a reduction of I_{Ca} density (I_{Ca} divided by cell capacitance) of 29.1% (Table 2). Their capacitance was smaller by 10% compared with wt IHCs with Ca^{2+} as a charge carrier, but not with Ba^{2+} as a charge carrier (Table 2). This discrepancy might result from reduced exocytosis in du/du IHCs in the Ca^{2+} current recordings (see below). Exocytosis, however, should not occur with Ba^{2+} as a charge carrier. Moreover, the V_h value was shifted by 5.2 mV to depolarized voltages in du/du IHCs, and the slope factor of I_{Ca} activation was increased by 0.9 mV, which indicates changed voltage-dependent gating of $Ca_v1.3$ channels lacking functional $\alpha_2\delta2$ subunits. Reduced peak I_{Ca} in du/du IHCs may result from (1) fewer $Ca_v1.3$ channels in du/du IHCs, (2) altered single-channel conductance, and (3) altered gating properties of I_{Ca} or a combination of items 1–3. The reason for item 3 is that a shift of the I_{Ca} activation curve toward positive voltage values not only increases V_h but also lowers peak I_{Ca} due to a reduced driving force. Therefore, the permeability density (permeability normalized to the cell capacitance; see Eq. 1 in Materials and Methods) was determined from fitting activation curves. On average, this parameter was significantly reduced by 22%, indicating a reduction of the product of the number of $Ca_v1.3$ channels × single-channel conductance of 22%.

Using Ba^{2+} as a charge carrier yielded larger currents (I_{Ba}) compared with Ca^{2+}, which is shown for a typical wt IHC and a typical du/du IHC from the apical turn (Fig. 2*D*,*E*). Averaged *I–V* curves demonstrated reduced peak I_{Ba} in apical (Fig. 2*F*) and medial du/du IHCs (Fig. 2*G*) compared with the respective wt IHCs. The average IHC I_{Ba} was significantly reduced by 29.1% (apical turn) and by 47.3% (medial turn); reduction of I_{Ba} density amounted to 29.1% for apical IHCs and to 39.0% for medial IHCs compared with wt IHCs of the respective cochlear location (Table 2). Fitting the *I–V* curves yielded a highly significant shift of V_h by 7.2 mV versus wt IHCs in apical du/du IHCs and by 7.8 mV in medial du/du IHCs, and the slope factor showed a tendency to larger values, which was significant for apical IHCs (Table 2). In sum, the effects of the ducky mutation on IHC Ca^{2+} channels were more severe in the medial turn compared with the apical turn, in accordance with the larger ABR threshold elevation in the middle frequencies (Fig. 1*A*).

Using depolarization steps lasting 400 ms, we tested Ca^{2+}- and voltage-dependent inactivation in apical turn IHCs. Peak current traces for wt and du/du IHCs are shown for I_{Ca} and I_{Ba} (Fig. 2*H*,*I*, respectively). The percentage of I_{Ca} inactivation after 300 ms was not different between wt and du/du IHCs, and the same was true for I_{Ba} (Table 2). Fitting I_{Ca} (I_{Ba}) traces with monoexponential functions yielded no difference in the inactivation time constants between wt and du/du apical IHCs for both I_{Ca} and I_{Ba} (Table 2).

Together, du/du IHCs showed significantly smaller I_{Ca} and I_{Ba} amplitudes and a positive shift in V_h. The rightward shift of the *I–V* curves by 5–8 mV in the absence of functional $\alpha_2\delta2$ demonstrates that $\alpha_2\delta2$ is part of the $Ca_v1.3$ channel complex and has a clear impact on channel gating in wt IHCs.

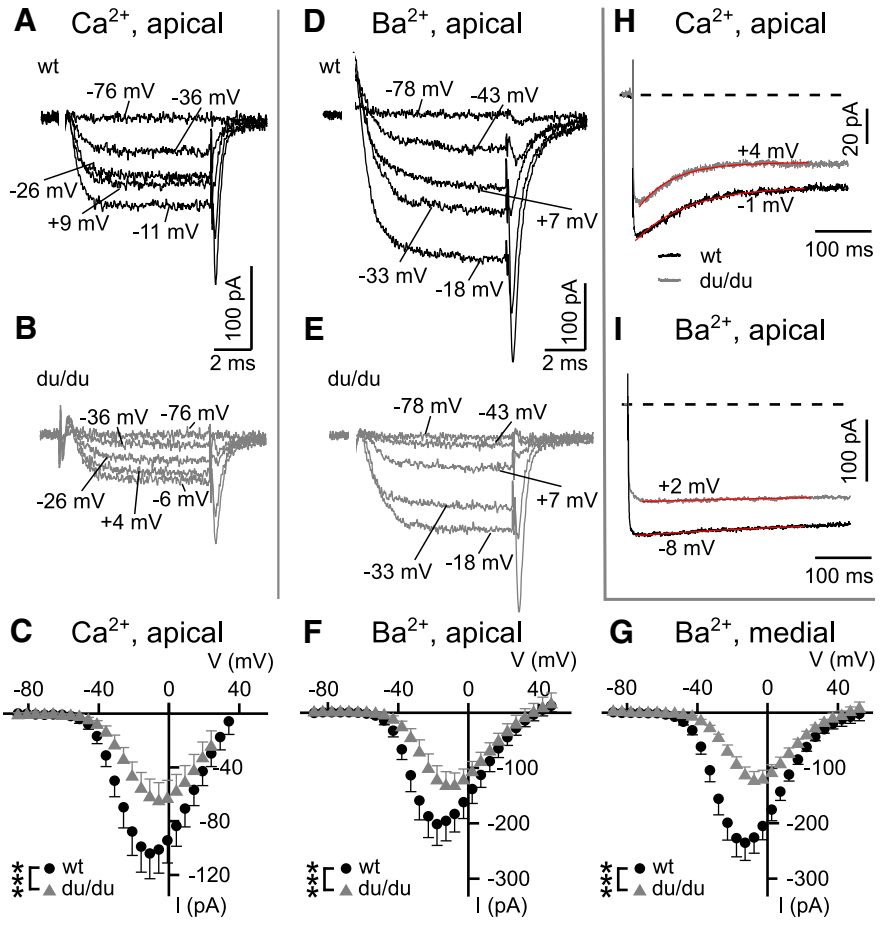

Figure 2. Whole-cell Ca^{2+} and Ba^{2+} currents in 3-week-old IHCs of ducky mice. ***A***, ***B***, Representative Ca^{2+} currents (I_{Ca}) of a wt IHC (***A***) and a du/du IHC (***B***) of apical cochlear turns in response to 8 ms step depolarizations to the voltages indicated. ***C***, Averaged Ca^{2+} *I–V* curves ± SD for 20 apical turn wt and 12 apical turn du/du IHCs. For clarity, the SD is plotted in one direction only (−SD or +SD). Two-way ANOVA for the effect of genotype, $^{***}p < 0.001$. ***D***, ***E***, Representative Ba^{2+} currents (I_{Ba}) of a wt (***D***) and a du/du IHC (***E***) of apical cochlear turns in response to 8 ms step depolarizations to the voltages indicated. ***F***, Averaged Ba^{2+} *I–V* curves ± SD for 12 apical turn wt and 11 apical turn du/du IHCs. Two-way ANOVA for the effect of genotype, $^{***}p < 0.001$. ***G***, Averaged Ba^{2+} *I–V* curves ± SD for 13 wt and 9 du/du IHCs of medial/midbasal turns. Two-way ANOVA for the effect of genotype, $^{***}p < 0.001$. ***H***, I_{Ca} responses to step depolarizations to V_{max} lasting 400 ms and monoexponential fits (red) in a wt and a du/du IHC of apical cochlear turns. ***I***, I_{Ba} responses to step depolarizations to a V_{max} lasting 400 ms and monoexponential fits (red) in an apical wt and an apical du/du IHC.

Reduced exocytosis with normal Ca^{2+} efficiency in IHCs of du/du mice

Next, we asked how the altered Ca^{2+} currents affected exocytosis in IHCs of du/du mice. Apical IHCs of mice aged P18–P20 were held at −85 mV, stimulated with 100 ms steps to different voltages, and changes in membrane capacitance (ΔC_m) reflecting exocytosis were determined with 5 mM Ca^{2+} as a charge carrier (Fig. 3). Figure 3*A* depicts typical ΔC_m increases (middle) and corresponding I_{Ca} traces (bottom) upon stepping to the individual V_{max} for a wt and a du/du IHC. Both the capacitance increase and the underlying I_{Ca} were smaller in the du/du IHC. Capacitance changes were also determined as a function of voltage between −85 and 45 mV in 10 mV steps. Averaged ΔC_m (top) and corresponding peak I_{Ca} values (bottom) as a function of voltage are shown for 10 wt and 11 du/du IHCs (Fig. 3*B*), yielding *C–V* and *I–V* curves. The *C–V* curves largely reflected the voltage dependence of the corresponding inverted *I–V* curves for both wt and du/du IHCs, with significant reductions of ΔC_m at −15 and −5 mV (Fig. 3*B*, top; two-way ANOVA, effect of genotype, $p < 0.05$), the range of the largest differences in I_{Ca} between genotypes (Fig. 3*B*, bottom). To assess the Ca^{2+} efficiency of exocytosis, the Ca^{2+} charge Q_{Ca} was calculated by integrating the absolute value of I_{Ca} over the time of depolarization, including tail currents in the ascending part of the *C–V* (up to 5 mV), and averaged ΔC_m values were plotted against Q_{Ca} (Fig. 3*C*). Fits corresponding to Equation 6 yielded an averaged power N of 1.58 ± 0.20 (mean ± SEM) for 11 wt IHCs, which was not different from the power of 1.45 ± 0.13 (mean ± SEM; $p = 0.62$, Student's t test) for 10 du/du IHCs. Thus, the Ca^{2+} efficiency of exocytosis was unchanged in du/du IHCs, and the reduction of ΔC_m between −15 and −5 mV in du/du IHCs (Fig. 3*B*, top) was a result of their correspondingly reduced Ca^{2+} currents (between −25 and +5 mV; Fig. 3*B*, bottom).

Expression of BK channels in du/du mice

The presence of Ca^{2+}- and voltage-dependent BK channels is a hallmark of mature IHCs. Their expression starts at the onset of hearing (Kros et al., 1998; Hafidi et al., 2005) and requires the presence of substantial $Ca_v1.3$ currents in neonatal development, because BK currents are absent from $Ca_v1.3^{-/-}$ IHCs (Brandt et al., 2003) and altered in IHCs lacking $Ca_v\beta2$ (Neef et al., 2009). Because mature du/du IHCs from the apical turn revealed a reduction of peak I_{Ca} by 37%, we analyzed BK currents and protein expression of the pore-forming subunit BKα (Fig. 4). Typical whole-cell outward currents are shown for a wt (Fig. 4*A*) and a du/du apical IHC (Fig. 4*B*). *I–V* curves were extracted from current families by averaging the current amplitudes between 1.2 and 1.3 ms after the start of the depolarization (I_{fast}; Fig. 4*A*,*B*), at a time when delayed rectifier K^+ currents are not yet activated (Brandt et al., 2007), and plotting them as a function of voltage (Fig. 4*C*). *I–V* curves were fitted by a first-order Boltzmann function, yielding the activation parameters V_h and k. Neither the average current amplitude nor the current density (both determined at 0 mV) and the activation parameters (V_h, k) were altered in du/du mice (Table 3). Activation kinetics of I_{fast} was fitted by monoexponential functions from 0.3 to 0.5 ms after the start of depolarization between −25 and 10 mV (Fig. 4*A*,*B*, red curves). The resulting averaged activation time constants of du/du IHCs were slightly larger over the voltage range analyzed than those of wt IHCs, indicating that BK currents activated slightly slower in du/du IHCs at a given voltage (Fig. 4*D*; two-way ANOVA, $p < 0.01$). A similar subtle increase in activation time constants has been observed in a subset of hypothyroid IHCs, which expressed BK currents with a developmental delay of 2 weeks (Brandt et al., 2007). In du/du IHCs, BKα protein showed a normal localization at the neck of the IHCs (red dot-like labeling; Fig. 4*E*,*F*). Together, BK current amplitudes, *I–V* relations, and localization of BKα were normal in du/du IHCs.

Table 2. Ca^{2+}/Ba^{2+} current amplitudes, membrane capacitances, and activation and inactivation parameters of I_{Ca} and I_{Ba} in mature IHCs of du/du mice

	Apical coil, Ca^{2+} currents		Apical coil, Ba^{2+} currents		Medial coil, Ba^{2+} currents	
Parameters	wt ($n = 20$)	du/du ($n = 12$)	wt ($n = 12$)	du/du ($n = 11$)	wt ($n = 13$)	du/du ($n = 9$)
$\lvert I_{max}\rvert$ (pA)	103.8 ± 18.2	65.1 ± 14.0***	201.6 ± 38.3	142.9 ± 29.6**	235.3 ± 32.1	123.9 ± 17.3***
C_m (pF)	10.2 ± 1.4	9.2 ± 1.1*	9.5 ± 1.2	9.6 ± 0.7	11.2 ± 1.0	9.7 ± 1.8*
$\lvert I_D\rvert$ (pA/pF)	10.3 ± 1.5	7.3 ± 2.1***	21.3 ± 3.6	15.1 ± 3.8**	21.3 ± 4.8	13.0 ± 2.2***
V_h (mV)	−26.5 ± 2.3	−21.3 ± 2.9***	−33.3 ± 1.5	−26.1 ± 3.4***	−29.7 ± 1.3	−21.9 ± 1.5***
k (mV)	11.4 ± 1.0	12.3 ± 0.9*	9.1 ± 0.5	9.8 ± 0.8*	10.0 ± 0.7	10.4 ± 0.5
Inactivation	wt ($n = 13$)	du/du ($n = 12$)	wt ($n = 10$)	du/du ($n = 9$)		
Inactivation after 300 ms (%)	32.3 ± 10.4	27.4 ± 7.9	10.0 ± 5.6	5.6 ± 2.4		
τ (ms)	158.4 ± 75.0	125.1 ± 70.8	380.4 ± 142.7	501.6 ± 190.9		

Membrane capacitances and voltage-dependent activation parameters of I_{Ca} and I_{Ba} in mature IHCs of wt and du/du mice. $\lvert I_{max}\rvert$, Absolute value of maximum current; C_m, membrane capacitance; $\lvert I_D\rvert$, absolute value of maximum current density. V_h values and the slope factor k were obtained from fitting I–V curves (see Materials and Methods, Eq. 1). All values are given as the mean ± SD.

*$p < 0.05$, **$p < 0.01$, ***$p < 0.001$.

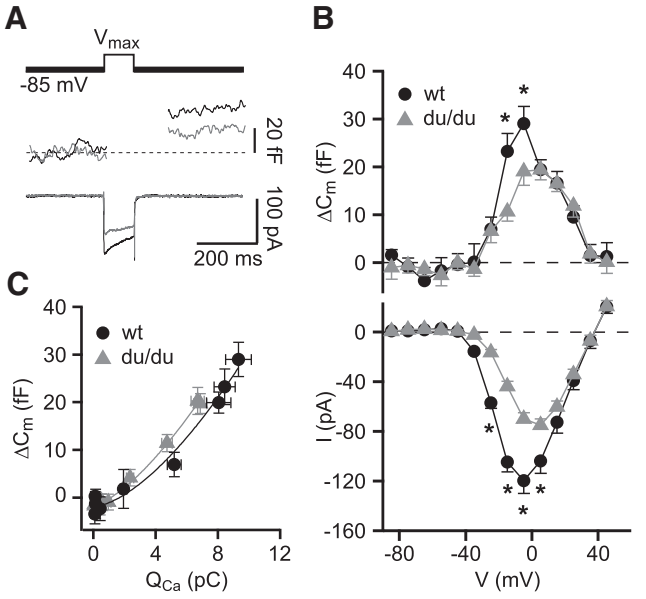

Figure 3. Reduced exocytosis with normal Ca^{2+} efficiency in IHCs of du/du mice. ***A***, Example traces of a P18 wt IHC and a P18 du/du IHC of apical turns. Cells were depolarized from V_h (−85 mV) for 100 ms to V_{max} (wt, −5 mV; du/du, +6 mV). Top, Stimulus protocol; middle, resulting ΔC_m; bottom, corresponding I_{Ca}. ***B***, Averaged ΔC_m ± SEM (top) and corresponding I_{Ca} ± SEM (bottom) as a function of voltage of 10 wt and 11 du/du IHCs. For clarity, the SEM is plotted in one direction only (−SEM or +SEM). Two-way ANOVA for the effect of genotype, *$p < 0.05$. ***C***, Averaged ΔC_m ± SEM plotted against the corresponding Ca^{2+} charge Q_{Ca} ± SEM. Q_{Ca} was calculated by integrating the absolute value of I_{Ca} over the time of depolarization, including the tail currents. Values for ΔC_m and I_{Ca} were taken from ***B*** between −75 mV (sometimes −55 mV) and 5 mV. Fits corresponding to Equation 6 to the individual curves yielded averaged powers N of 1.58 (wt, $n = 11$) and 1.45 (du/du, $n = 10$).

Table 3. Amplitudes and biophysical properties of BK currents in mature IHCs of du/du mice

Parameters	wt ($n = 10$)	du/du ($n = 8$)
I_{fast} at 0 mV (nA)	4.1 ± 1.4	3.8 ± 0.8
C_m (pF)	9.0 ± 1.0	8.3 ± 1.3
$I_{fast,D}$ at 0 mV (nA/pF)	0.46 ± 0.13	0.47 ± 0.13
V_h (mV)	4.1 ± 5.8	3.4 ± 5.8
k (mV)	14.3 ± 1.4	13.6 ± 1.2

All values are given as the mean ± SD. I_{fast} reflects the BK current and was fitted with a first-order Boltzmann function × driving force (Eq. 4), yielding voltages of half-maximum activation, V_h, and the slope factor k. $I_{fast,D}$, respective current density. None of the parameters differed significantly between the genotypes.

Presynaptic localization of $Ca_v1.3$ and $Ca_v\beta 2$ protein clusters is normal in du/du IHCs

Because of reduced Ca^{2+} currents in du/du IHCs, we asked whether the spatial distribution of the pore-forming $Ca_v1.3$ sub-

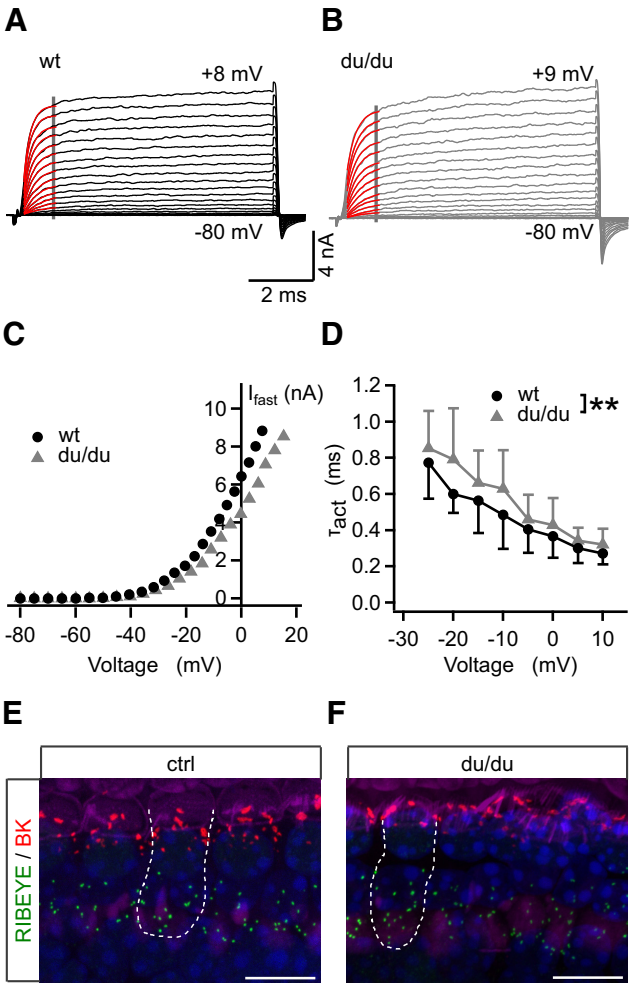

Figure 4. BK currents and the expression of BKα protein in du/du mice. ***A***, ***B***, Typical outward currents in IHCs from the apical turn of a wt mouse (***A***, P21) and a du/du mouse (***B***, P20) in response to voltage steps of 8 ms duration. Red traces are monoexponential fits to the current traces. ***C***, Corresponding I–V curves for the wt and du/du IHCs in ***A*** and ***B*** were obtained by averaging the current amplitudes from 1.2 to 1.3 ms after the start of depolarization (***A***, ***B***, gray lines), which represent K^+ currents through BK channels. ***D***, Average activation time constants ± SD of BK currents obtained from monoexponential fits from 0.3 to 0.5 ms as a function of voltage for 10 wt and 8 du/du mice; **$p < 0.01$, two-way ANOVA for the effect of genotype. ***E***, ***F***, Double immunolabeling for BKα (red) and the ribbon marker CtBP2/RIBEYE (green) in whole-mount preparations of organs of Corti from apical cochlear turns. Maximum intensity projections of confocal stacks of a stretch of four IHCs are shown for wt (***E***) and du/du (***F***). The dashed line shows the outline of an IHC, respectively. Nuclei are stained in blue with DAPI, and stereocilia and cuticular plates are stained with phalloidin (purple). Scale bar, 10 μm.

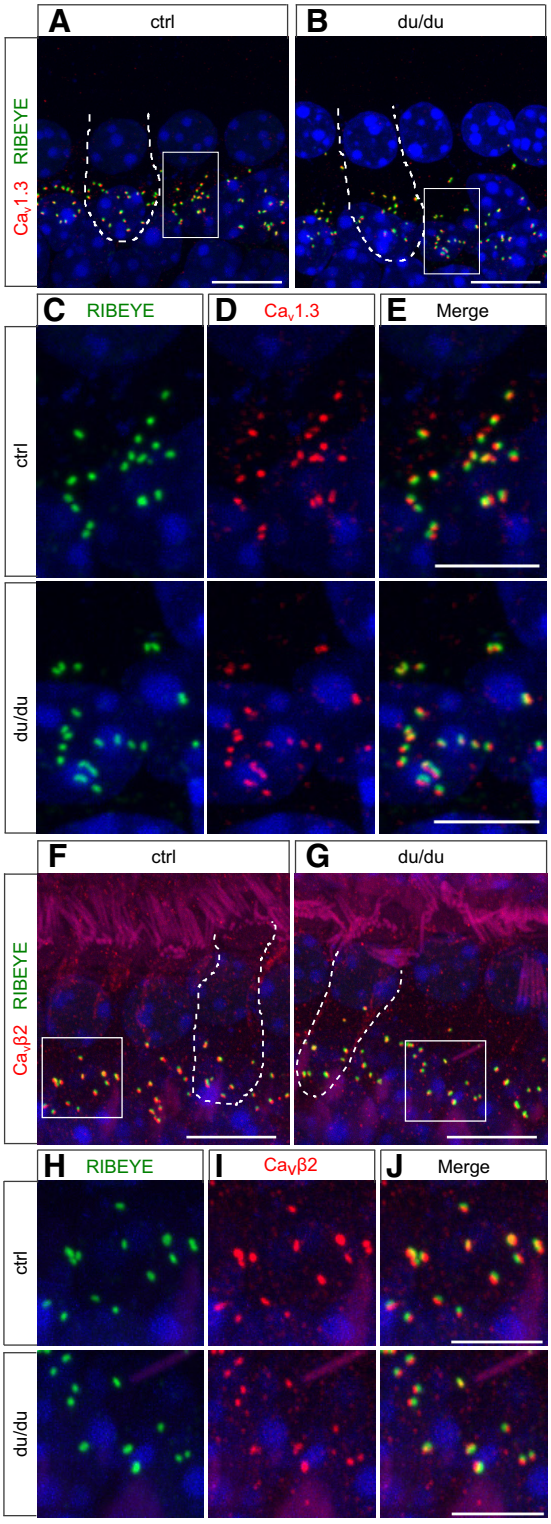

Figure 5. Expression of $Ca_v1.3$ and $Ca_v\beta2$ protein in IHCs of ducky mice. ***A–J***, MIP of confocal stacks of whole-mount preparations of organs of Corti from apical cochlear turns coimmunolabeled for $Ca_v1.3$ (***A–E***) or $Ca_v\beta2$ (***F–J***) with the ribbon marker CtBP2/RIBEYE at P18-P25. ***A***, ***B***, Stretches with four IHCs of ctrl (***A***) and du/du mice (***B***) labeled with anti-$Ca_v1.3$ and anti-RIBEYE are shown, with one IHC indicated by the dashed outline. The synaptic poles of the IHCs boxed in ***A*** and ***B*** are shown enlarged and with split color channels in ***C*** and ***D***. ***C***, Synaptic ribbons labeled with anti-RIBEYE at the basolateral pole of a ctrl IHC (top) and a du/du IHC (bottom). ***D***, Corresponding immunolabeling for $Ca_v1.3$. ***E***, Overlay of the signals of ***C*** and ***D*** indicates the close apposition of $Ca_v1.3$ clusters and ribbons at the basolateral pole in both ctrl and du/du IHCs. ***F***, ***G***, Localization of $Ca_v\beta2$ (red) and RIBEYE immunolabeling (green) in stretches of four IHCs of ctrl (***F***) and du/du mice (***G***), with one IHC indicated by the dashed outline. Stereocilia are stained in purple with phalloidin. Boxed synaptic poles from ***F*** and ***G*** are shown enlarged and with split color channels in ***H*** (RIBEYE, green) and ***I*** ($Ca_v\beta2$, red) for a ctrl (top) and a du/du IHC (bottom). ***J***, Overlay of the signals of ***H*** and ***I*** indicates close apposition of $Ca_v\beta2$ clusters and ribbons at the basolateral pole in both the ctrl and du/du IHCs. Nuclei are stained in blue with DAPI. Scale bars: ***A***, ***B***, ***F***, ***G***, 10 μm; ***C–E***, ***H–J***, 5 μm.

unit and the dominant $Ca_v\beta$ subunit $Ca_v\beta2$ of IHC Ca^{2+} channel complexes were altered in du/du IHCs. In control IHCs, $Ca_v1.3$ showed some extrasynaptic and cytosolic immunolabeling, but the most obvious labeling was observed in clusters with partial overlap with the ribbons (Fig. 5*A*, *C–E*, top). The same labeling pattern was found in IHCs of du/du mice (Fig. 5*B–E*, bottom). Similarly to $Ca_v1.3$, $Ca_v\beta2$ immunolabeling clustered at the ribbon synapses of control IHCs with partial overlap of $Ca_v\beta2$ and RIBEYE fluorescence signals (Fig. 5*F*, *H–J*, top). Again, the same labeling pattern was detected in IHCs of du/du mice (Fig. 5*G–J*, bottom). Ribbon numbers were counted in MIPs of anti-RIBEYE immunolabeling (Fig. 5, compare *A–C*, *F–H*). The average number of ribbons, which amounted to 16.3 ± 3.1 per control IHC and 15.3 ± 3.4 per du/du IHC, was not different between the two groups ($p = 0.55$; ribbons counted in three to six IHCs each of seven apical turn specimens of six control and du/du mice, respectively). Together, the ducky mutation neither affected the cluster formation of both $Ca_v1.3$ and $Ca_v\beta2$ at the ribbon synapses nor altered the number of IHC ribbons.

The spatial coupling of presynaptic $Ca_v1.3$ channels with postsynaptic PSD-95 and AMPA receptor clusters is impaired in du/du mice

Next we analyzed the expression and localization of the postsynaptic marker PSD-95, which acts as the main scaffold for postsynaptic receptor complexes (for review, see Opazo et al., 2012). The sizes of PSD-95 clusters showed some variability in both genotypes (Fig. 6*A–C*). Quantification of PSD-95 cluster areas did not reveal a significant difference between control IHCs (0.43 ± 0.24 μm^2, $n = 572$) and du/du IHCs (0.47 ± 0.43 μm^2, $n = 747$; $p = 0.228$, Mann–Whitney *U* test). Double immunolabeling for $Ca_v1.3$ and PSD-95 revealed largely overlapping fluorescence signals in control mice, with the smaller $Ca_v1.3$ signals fully covered by the larger PSD-95 signals (Fig. 6*A*, *C–E*, top). Occasionally, a $Ca_v1.3$-labeled cluster was not accompanied by a PSD-95-positive spot. However, at du/du synapses, significantly more separated $Ca_v1.3$- and PSD-95-positive clusters were observed (Fig. 6*B–E*, bottom), which was further quantified using a line scan analysis (see Materials and Methods; Fig. 6*E*, *F*) applied on MIPs covering four to five IHCs, as shown in Figure 6, *A* and *B*. The average total number of PSD-95 and $Ca_v1.3$ clusters was not different between apical turn of control and du/du mice, respectively (Fig. 6*G*). In contrast, the number of both separated PSD-95 and separated $Ca_v1.3$ clusters was significantly increased at apical du/du IHC synapses (Fig. 6*H*). The same was true for IHCs of the medial turn (Fig. 6*I*, *J*). About 21% (18.5%) of all PSD-95 clusters and 11% (19.8%) of all $Ca_v1.3$ clusters were separated from the respective counterpart in apical (respectively medial) wt IHCs, whereas those numbers increased to 39% (49.5%) and 30% (50.9%) for du/du IHCs of the apical (respectively medial) cochlear turn. In other words, lack of functional $\alpha_2\delta2$ increased the number of unpaired PSD-95 clusters by a factor of 1.9 for the apical and 2.8 for the medial turn, and that of unpaired $Ca_v1.3$ clusters by a factor of 2.7 for both apical and medial turns. These findings indicate that the $\alpha_2\delta2$ subunit is

←

required for an optimal apposition of IHC presynaptic $Ca_v1.3$ channels and the postsynaptic scaffold protein PSD-95.

Postsynaptic AMPA receptors face the IHC synaptic cleft and could directly or indirectly interact with $\alpha_2\delta2$ at the $Ca_v1.3$ channel complex. AMPA receptors are (hetero-)tetramers consisting of four types of GluA1–4 subunits and auxiliary subunits (Traynelis et al., 2010); and GluA2/3 and GluA4 have been shown at the IHC synapse (Matsubara et al., 1996; Khimich et al., 2005; Engel et al., 2006). For double-labeling AMPA receptors and $Ca_v1.3$ channels, a goat polyclonal GluA4 antibody was chosen, which required ethanol fixation. $Ca_v1.3$ clusters partially overlapped with the larger GluA4 clusters or were completely enclosed by them in MIPs of the wt IHCs, but much less so in du/du IHCs, shown for the medial turn IHCs (Fig. 7). Figure 7, *A* and *B*, shows an overlay of red $Ca_v1.3$ and green GluA4 immunofluorescence in a region containing four wt and du/du IHCs, respectively. GluA4 clusters looked less ordered and somewhat fragmented (Fig. 7*B*,*D*,*E*) in du/du IHCs. Further, the number and size of $Ca_v1.3$ clusters was more variable, with a tendency to smaller sizes in du/du IHCs compared with wt IHCs, as shown in two examples of du/du IHCs with split color channels (Fig. 7*B*,*D*,*E*). A quantitative analysis demonstrated that the total number of GluA4-positive clusters was not different in du/du versus wt IHCs (Fig. 7*F*). Quantification of GluA4 clusters overlapping with $Ca_v1.3$ clusters yielded relatively small numbers when normalized to one IHC for the wt IHC (6.4 ± 3.7 per apical turn and 10.0 ± 4.7 per medial turn IHC; Fig. 7*G*). In our experience, using ethanol as a fixative generally results in smaller clusters of ion channels than using the cross-linking fixative PFA. Using a minimum size threshold in the subsequent analysis to discriminate signal from background may have contributed to an underestimation of the number of $Ca_v1.3$ clusters. However, in du/du IHCs the number of GluA4 clusters overlapping $Ca_v1.3$ clusters was further and significantly reduced ($p < 0.001$) to 3.6 ± 2.9 (per apical turn IHC) and to 4.3 ± 3.2 (per medial turn IHC) or to 56% of wt IHCs for the apical turn and 43% of wt IHCs for the medial turn (Fig. 7*G*).

In summary, the lack of functional $\alpha_2\delta2$ not only reduced the amplitude and shifted the voltage dependence of Ca^{2+} currents and exocytosis in IHCs, but, moreover, impaired the trans-synaptic apposition with GluA4 glutamate receptors and the postsynaptic scaffold PSD-95, which altogether led to hearing impairment.

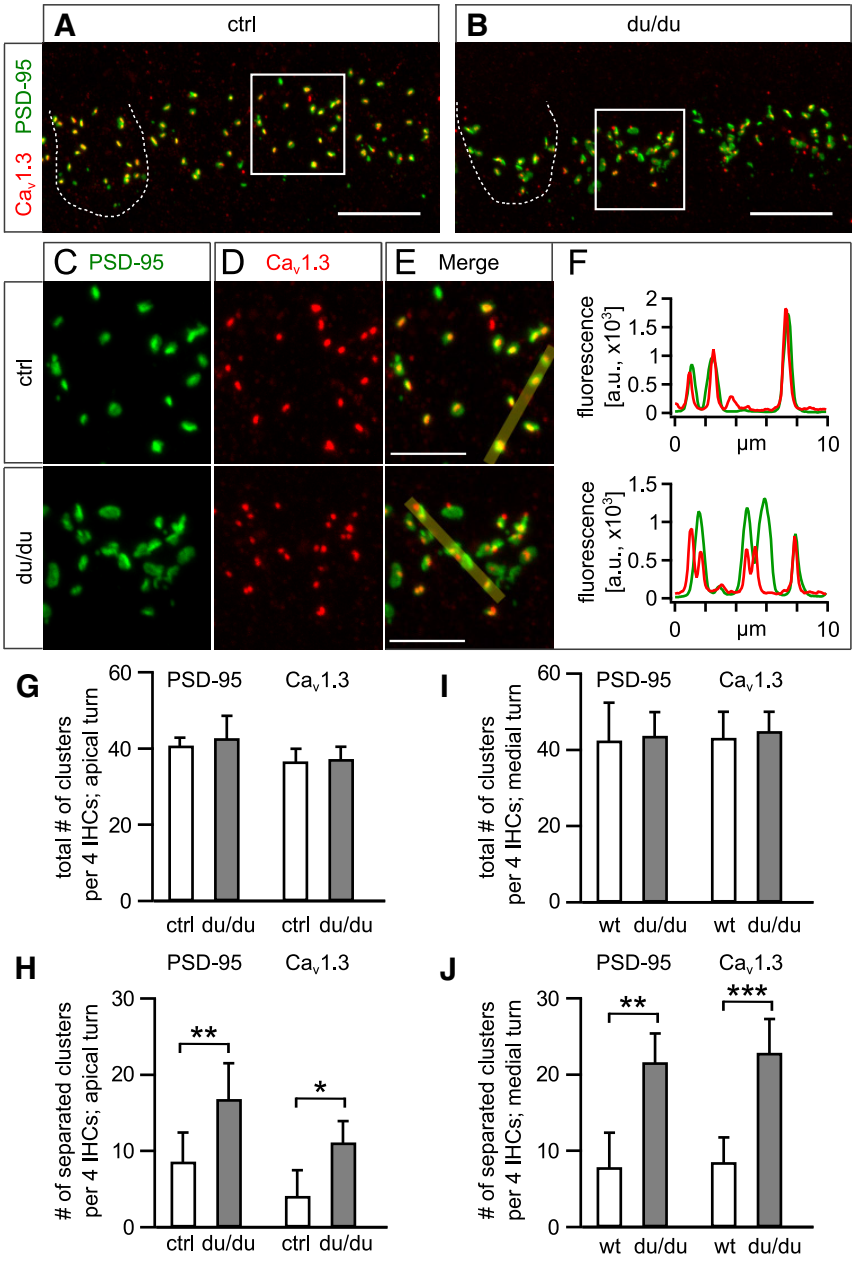

Figure 6. Altered spatial coupling of presynaptic $Ca_v1.3$ and postsynaptic PSD-95 clusters at the IHC synapse in du/du mice. ***A***, ***B***, MIP of confocal stacks of whole-mount preparations of organs of Corti from apical cochlear turns coimmunolabeled for $Ca_v1.3$ and PSD-95 at P19–P24. Stretches of four IHCs of a ctrl (***A***) and du/du mouse (***B***) labeled with anti-$Ca_v1.3$ (red) and anti-PSD-95 (green) are shown, with a synaptic pole of an IHC indicated by the dashed outline. ***C***, ***D***, Boxed synaptic poles from ***A*** and ***B*** are shown enlarged and with split color channels in ***C*** (PSD-95, green) and ***D*** ($Ca_v1.3$, red) for ctrl (top) and du/du IHC (bottom). ***E***, Merged images contain a bar tool (10 μm long, 0.7 μm wide) that is used for colocalization analysis. Scale bars: ***A***, ***B***, 10 μm; ***C–E***, 5 μm. ***F***, Fluorescence intensity profiles for $Ca_v1.3$ (red) and PSD-95 immunolabeling (green) for the corresponding bar tools in ***E*** as a function of length. ***G***, Analysis of the total number of immunopositive spots in regions each containing four apical turn IHCs covered by 10 bar tools, respectively, for PSD-95 ($p = 0.57$) and $Ca_v1.3$ labeling ($p = 0.81$) in ctrl IHCs ($n = 6/4$ ears/animals) and du/du IHCs ($n = 6/4$ ears/animals) revealed no difference between the genotypes. ***H***, Both the numbers of separated PSD-95 clusters and those of separated $Ca_v1.3$ clusters were significantly increased in apical du/du versus ctrl IHCs (*$p < 0.05$; **$p < 0.01$, Mann–Whitney *U* test). ***I***, Similarly, the total number of immunopositive spots for PSD-95 ($p = 0.24$) and $Ca_v1.3$ labeling ($p = 0.46$) in wt (specimen of 4 IHCs each, $n = 6/4$ ears/animals) and du/du medial turn IHCs ($n = 6/3$ ears/animals) showed no differences between genotypes. ***J***, Numbers of separated PSD-95 clusters and $Ca_v1.3$ clusters were significantly increased in medial turn du/du vs wt IHCs (**$p < 0.01$; ***$p < 0.001$, Mann–Whitney *U* test).

Discussion

Using the ducky mouse lacking functional $\alpha_2\delta2$, we show here with voltage-clamp recordings that $\alpha_2\delta2$ coassembles with $Ca_v1.3$ and $Ca_v\beta2$ in wt IHCs. It regulates the Ca^{2+} cur-

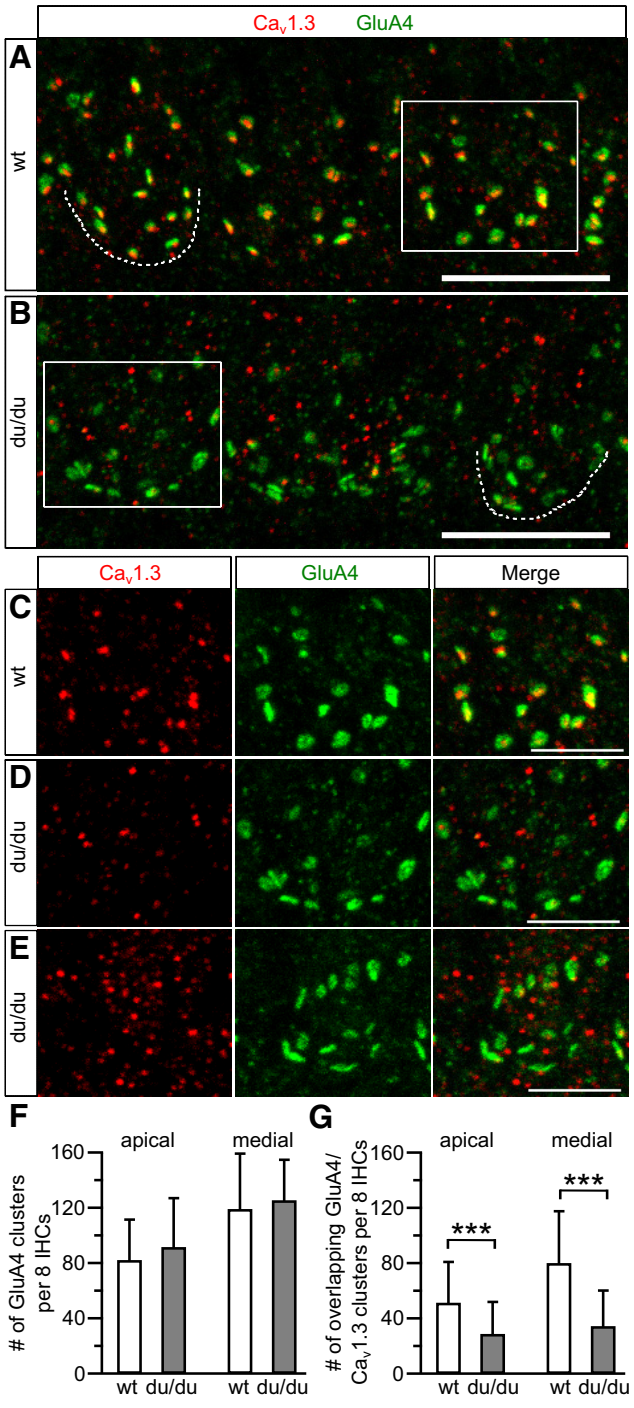

Figure 7. Impaired spatial coupling of presynaptic $Ca_v1.3$ clusters and postsynaptic GluA4 AMPA receptor clusters at the IHC synapse in du/du mice. ***A***, ***B***, MIP of confocal stacks of whole-mount preparations of organs of Corti from medial cochlear turns coimmunolabeled for $Ca_v1.3$ and GluA4 at P22–P23. Stretches with three to four IHCs of a wt (***A***) and du/du mouse (***B***) labeled with anti-$Ca_v1.3$ (red) and anti-GluA4 (green) are shown, with the synaptic pole of one IHC indicated by the dashed outline. ***C–E***, Boxed synaptic poles of IHCs from ***A*** and ***B*** are shown enlarged with color channels split in red ($Ca_v1.3$, left column) and green (GluA4, middle column), and with merged colors (left column) for wt (***C***) and du/du mice (***D***, ***E***). ***F***, ***G***, Quantitative analysis of the spatial overlap of $Ca_v1.3$ and GluA4 immunolabeling in specimen, each containing a stretch of eight IHCs. ***F***, The total number of GluA4-positive clusters was unchanged at IHC postsynapses of both the apical ($p = 0.084$) and the medial cochlear turn in du/du mice ($p = 0.29$). ***G***, The numbers of overlapping $Ca_v1.3$/GluA4 clusters were significantly decreased in du/du vs wt IHCs from both apical and medial cochlear turns. ***$p < 0.001$, Mann–Whitney *U* test. Number of ears/animals/specimens analyzed (with eight IHCs per specimen), respectively: wt: apical, 10/6/53; medial, 8/6/40; du/du: apical, 7/4/42; medial, 7/4/36. Scale bars: ***A***, ***B***, 10 μm; ***C–E***, 5 μm.

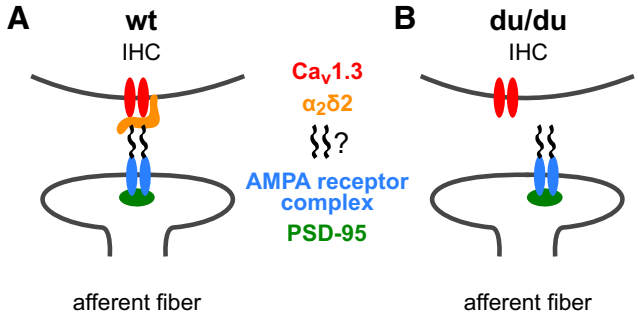

Figure 8. Model of the role of $\alpha_2\delta2$ in trans-synaptic coupling of IHC $Ca_v1.3$ channels with the postsynaptic AMPA receptor complex. ***A***, In the wt IHC, the extracellularly localized $\alpha_2\delta2$ subunit (orange) couples the $Ca_v1.3$ channel (red) with the AMPA receptor complex (blue), possibly through an unknown linker protein (black). PSD-95 (green) acts as a scaffold for AMPA receptors. The $\alpha_2\delta2$-mediated trans-synaptic link perfectly aligns the presynaptic $Ca_v1.3$ channel with the postsynaptic AMPA receptor–PSD-95 complex. ***B***, In du/du mice lacking functional $\alpha_2\delta2$, the coupling between $Ca_v1.3$ channels and the AMPA receptor complex is abolished. As a result, the AMPA receptor–PSD-95 complex is no longer perfectly aligned with $Ca_v1.3$ across the synaptic cleft, leading to an increase in the number of separated $Ca_v1.3$ and GluA4/PSD-95 clusters, respectively.

rent amplitude and has an impact on the gating of $Ca_v1.3$ channels.

$\alpha_2\delta$ subunits in hair cells

Real-time qPCR analysis of all $\alpha_2\delta$ subunit isoforms indicated that neonatal IHCs express mainly $\alpha_2\delta2$, whereas mature IHCs exclusively express $\alpha_2\delta2$ mRNA. The low expression of $\alpha_2\delta3$ mRNA detected in IHCs before hearing onset is in accordance with a small reduction of the Ba^{2+} current density in immature IHCs of $\alpha_2\delta3^{-/-}$ mice (Pirone et al., 2014). $\alpha_2\delta2$ mRNA was clearly present in both immature and mature IHCs and OHCs. Its low level at P20–P25 can be explained by the downregulation of $Ca_v1.3$ currents during development to only one-third of the level present at P6 in IHCs (Beutner and Moser, 2001; Johnson et al., 2005) and similarly also in OHCs (Knirsch et al., 2007). The fact that $\alpha_2\delta1$, $\alpha_2\delta3$, and $\alpha_2\delta4$ mRNA were not detected indicates that $\alpha_2\delta2$ is the dominant $\alpha_2\delta$ isoform that forms Ca^{2+} channels with $Ca_v1.3$ and $Ca_v\beta2$ in mature IHCs. Interestingly, this L-type channel complex ($Ca_V1.3/\beta2/\alpha_2\delta2$) is distinct from the P/Q-type channel complex in cerebellar Purkinje cells, which also coassembles with $\alpha_2\delta2$ ($Ca_v2.1/\beta4/\alpha_2\delta2$; Barclay et al., 2001). Given that in hair cells $Ca_v1.3$ currents are indispensable for generating Ca^{2+} action potentials, changes in immature Ca^{2+} currents may alter aspects of IHC development, leading, for example, to altered BK current properties in $Ca_v\beta2^{-/-}$ IHCs (Neef et al., 2009) and du/du IHCs (see below).

$Ca_v1.3$ channels and $Ca_v\beta2$ subunits still reached the IHC membrane and clustered at ribbon synapses of du/du IHCs. From our whole-cell recordings, we cannot determine whether the number of $Ca_v1.3$ channels, the single-channel conductance, or both were reduced. It is more likely, however, that the number of $Ca_v1.3$ channels present at the IHC surface rather than the single-channel conductance was affected. Immunolabeling showed smaller $Ca_v1.3$ clusters at du/du IHC presynapses, which were visible with the non-cross-linking ethanol fixation (Fig. 7), suggesting fewer $Ca_v1.3$ channels in the IHC membrane. Second, the single-channel conductance of $Ca_v2.1$ channels was unchanged both in cultured neonatal du/du Purkinje cells and in COS cells transfected with $Ca_v2.1/Ca_v\beta4$ and ducky-$\alpha_2\delta2$ compared with the respective wt (Barclay et al., 2001; Brodbeck et al.,

2002). Based on a reduced surface expression of Ca^{2+} channels, du/du Purkinje neurons showed a 35% reduction of the whole-cell Ba^{2+} current (Barclay et al., 2001), which was similar to the reduction of the du/du IHC whole-cell Ca^{2+}/Ba^{2+} current amplitude by 30–40% reported here. Impaired trans-synaptic coupling due to a lack of functional $\alpha_2\delta2$ in the du/du IHC may have led to a reduced stability and increased turnover of $Ca_v1.3$ in the membrane (Dolphin, 2013) and, hence, a reduction of the Ca^{2+}/Ba^{2+} current (see below).

Coassembly of $Ca_v1.3$ with $\alpha_2\delta2$ at IHC ribbon synapses is surprising because $\alpha_2\delta4$ together with $Ca_v1.4$ and $Ca_v\beta2$ forms presynaptic L-type Ca^{2+} channel complexes at ribbon synapses of retinal photoreceptor and bipolar cells (De Sevilla Müller et al., 2013). Mice with a mutation of *Cacna2d4* exhibit cone–rod dysfunction (Wycisk et al., 2006a), and humans with mutations in *CACNA2D4* have autosomal-recessive cone dystrophy (Wycisk et al., 2006b). A potential contribution of $\alpha_2\delta2$ to L-type Ca^{2+} channels at retinal ribbon synapses has yet to be established.

$\alpha_2\delta2$ and hearing

Ducky mice exhibited elevated ABR thresholds, which is in line with reduced Ca^{2+} currents and reduced exocytosis in the IHCs. Unexpectedly, their elevated ABR thresholds were accompanied by DPOAEs with amplitudes that are larger than normal (Fig. 1*A*,*B*). There are cases of severe auditory neuropathy where deafness coexists with partially normal DPOAEs, such as in humans with mutations in otoferlin (Rodríguez-Ballesteros et al., 2003; Tekin et al., 2005) or in mice deficient in $Ca_v1.3$ (Engel et al., 2006). Given that the reduction of I_{Ca} in du/du IHCs at any given voltage was ~50% compared with wt IHCs, the increase in click or frequency ABR thresholds of du/du mice was unexpectedly mild. Two scenarios, both of which are based on the systemic ablation of functional $\alpha_2\delta2$ in du/du mice, may have reduced the hearing loss. First, the stapedius reflex, a middle ear reflex, attenuates loud sound entering the ear (Mukerji et al., 2010). If $\alpha_2\delta2$ was playing an important role in transmitter release at the neuromuscular junction of the stapedius muscle in wt mice, that reflex may have been attenuated in du/du mice, increasing the sound amplitude entering the cochlea and the DPOAE signal leaving the cochlea. Alternatively, inhibitory synapses at OHCs, which are activated at medium to high sound pressure levels (for review, see Guinan, 2006), could require $\alpha_2\delta2$-containing presynaptic Ca^{2+} channels for transmitter release, which would result in impaired inhibition of OHCs in du/du mice. Disinhibition of the cochlear amplifier would alleviate an otherwise substantial hearing loss, inferred from altered function of the du/du IHCs alone. To assess the isolated, IHC-dependent contribution of $\alpha_2\delta2$ to hearing function will require the analysis of a conditional, IHC-specific $\alpha_2\delta2$ knock-out mouse, in which systemic effects of $\alpha_2\delta2$ deletion on other synapses (e.g., of brainstem medial efferent olivocochlear or stapedius nerve fibers) can be excluded.

The drugs gabapentin and pregabalin targeting $\alpha_2\delta1$ und $\alpha_2\delta2$ are used for the treatment of neuropathic pain and epilepsy in humans (Dolphin, 2012b). They likely reduce the number of functional Ca^{2+} channels by interfering with their trafficking from the ER to the plasma membrane (Hendrich et al., 2008; Tran-Van-Minh and Dolphin, 2010). Reversible hearing loss has been reported as a side effect of gabapentin treatment under conditions of elevated plasma concentrations (Pierce et al., 2008), which may have been caused by a severe reduction of $Ca_v1.3$ channels/currents in IHC membranes.

A novel function of $\alpha_2\delta2$ at the IHC synapse

IHCs of du/du mice exhibited a largely normal phenotype with respect to cell capacitance (i.e., cell size), amplitude of whole-cell BK currents, localization of BK channels, number of ribbons, and clustering of $Ca_v1.3$ and $Ca_v\beta2$ protein at the ribbons. The shift in V_h of the Ca^{2+} currents in du/du IHCs, being equivalent to altered gating of $Ca_v1.3$ channels, strongly suggests that in wt IHCs the extracellularly localized $\alpha_2\delta2$ subunit physically interacts with the extracellular loops of the $Ca_v1.3$ protein (Dolphin, 2013). Synapses of the afferent auditory pathway require ultrafast synaptic transmission, and optimal positioning of presynaptic release sites and postsynaptic receptor complexes is an important factor in keeping reaction times short. Here we have shown that trans-synaptic alignment of $Ca_v1.3$ clusters with GluA4 AMPA receptors and with the postsynaptic scaffold PSD-95 was impaired at IHC synapses lacking functional $\alpha_2\delta2$. In general, presynaptic and postsynaptic neuronal compartments in the CNS are coupled by the cell adhesion molecules neuroligin and neurexin, which form an interaction layer in the synaptic cleft (Südhof, 2008). Presynaptic neurexins are anchored at the active zone, whereas neuroligins are anchored at the postsynaptic density (Südhof, 2008). Ablation of all three neurexin isoforms led to a marked reduction of presynaptic $Ca_v2.2$ currents in neocortical neurons (Missler et al., 2003), but the mechanism for this link is unclear. If neurexins/neuroligins are expressed at the IHC synapse, which is unknown so far, they may be responsible for the principal organization of the synapse, whereas $\alpha_2\delta2$ might contribute to fine-tuning the apposition of clustered $Ca_v1.3$ channels and postsynaptic elements, such as GluA4 and PSD-95, for reducing reaction times (Figs. 6, 7, 8). $\alpha_2\delta$ subunits bear protein–protein interaction domains, including a von Willebrand factor A domain and a Cache domain (Dolphin, 2012a, 2013), which makes them good candidates for coupling Ca_v subunits (with which they interact noncovalently) with proteins of the AMPA receptor complex directly or with proteins of the extracellular matrix (Eroglu et al., 2009; Fig. 8). Recently, the extracellular matrix proteins thrombospondin 1 and 2 have been shown to be required for proper IHC synaptogenesis (Mendus et al., 2014). $\alpha_2\delta1$ has been shown to act as a receptor for thrombospondins independently of its contribution to Ca^{2+} channel function (Eroglu et al., 2009), and $\alpha_2\delta2$ might have a similar function.

From our findings, the question arises as to whether $\alpha_2\delta$ subunits, specifically $\alpha_2\delta2$, play a role in coupling presynaptic VGCCs and postsynaptic receptors, not only in IHCs, but also at CNS synapses. Because of the uniform pore-forming subunit $Ca_v1.3$ and the unusual clustering of ~80 $Ca_v1.3$ channels at each IHC presynapse (Brandt et al., 2005), the highly specialized IHC may enable us to dissect functions of $\alpha_2\delta$ subunits and possibly other presynaptic and postsynaptic partners, which at conventional synapses—due to the much smaller active zones—so far have remained elusive. Here we show that $\alpha_2\delta2$ can form Ca^{2+} channel complexes not only with $Ca_v2.1$ and $Ca_v\beta4$, as in cerebellar Purkinje cells (Barclay et al., 2001), but also with the L-type channel $Ca_v1.3$ and auxiliary $Ca_v\beta2$ (Neef et al., 2009). In conclusion, the specific combination of a particular pore-forming $Ca_v\alpha_1$ subunit with a distinct $\alpha_2\delta$ isoform *in vivo* may be determined by the requirements of the synapse rather than by the α_1 subunit itself.

References

Baig SM, Koschak A, Lieb A, Gebhart M, Dafinger C, Nürnberg G, Ali A, Ahmad I, Sinnegger-Brauns MJ, Brandt N, Engel J, Mangoni ME, Farooq M, Khan HU, Nürnberg P, Striessnig J, Bolz HJ (2011) Loss of Ca(v)1.3

(CACNA1D) function in a human channelopathy with bradycardia and congenital deafness. Nat Neurosci 14:77–84. CrossRef Medline

Barclay J, Balaguero N, Mione M, Ackerman SL, Letts VA, Brodbeck J, Canti C, Meir A, Page KM, Kusumi K, Perez-Reyes E, Lander ES, Frankel WN, Gardiner RM, Dolphin AC, Rees M (2001) Ducky mouse phenotype of epilepsy and ataxia is associated with mutations in the Cacna2d2 gene and decreased calcium channel current in cerebellar Purkinje cells. J Neurosci 21:6095–6104. Medline

Beutner D, Moser T (2001) The presynaptic function of mouse cochlear inner hair cells during development of hearing. J Neurosci 21:4593–4599. Medline

Brandt A, Striessnig J, Moser T (2003) $Ca_v1.3$ channels are essential for development and presynaptic activity of cochlear inner hair cells. J Neurosci 23:10832–10840. Medline

Brandt A, Khimich D, Moser T (2005) Few $Ca_v1.3$ channels regulate the exocytosis of a synaptic vesicle at the hair cell ribbon synapse. J Neurosci 25:11577–11585. CrossRef Medline

Brandt N, Kuhn S, Münkner S, Braig C, Winter H, Blin N, Vonthein R, Knipper M, Engel J (2007) Thyroid hormone deficiency affects postnatal spiking activity and expression of Ca^{2+} and K^+ channels in rodent inner hair cells. J Neurosci 27:3174–3186. CrossRef Medline

Brill J, Klocke R, Paul D, Boison D, Gouder N, Klugbauer N, Hofmann F, Becker CM, Becker K (2004) entla, a novel epileptic and ataxic Cacna2d2 mutant of the mouse. J Biol Chem 279:7322–7330. CrossRef Medline

Brodbeck J, Davies A, Courtney JM, Meir A, Balaguero N, Canti C, Moss FJ, Page KM, Pratt WS, Hunt SP, Barclay J, Rees M, Dolphin AC (2002) The ducky mutation in Cacna2d2 results in altered Purkinje cell morphology and is associated with the expression of a truncated alpha 2 delta-2 protein with abnormal function. J Biol Chem 277:7684–7693. CrossRef Medline

Catterall WA (2000) Structure and regulation of voltage-gated Ca2+ channels. Annu Rev Cell Dev Biol 16:521–555. CrossRef Medline

Cole RL, Lechner SM, Williams ME, Prodanovich P, Bleicher L, Varney MA, Gu G (2005) Differential distribution of voltage-gated calcium channel alpha-2 delta (alpha2delta) subunit mRNA-containing cells in the rat central nervous system and the dorsal root ganglia. J Comp Neurol 491:246–269. CrossRef Medline

Davies A, Hendrich J, Van Minh AT, Wratten J, Douglas L, Dolphin AC (2007) Functional biology of the alpha(2)delta subunits of voltage-gated calcium channels. Trends Pharmacol Sci 28:220–228. CrossRef Medline

De Sevilla Müller LP, Liu J, Solomon A, Rodriguez A, Brecha NC (2013) Expression of voltage-gated calcium channel alpha(2)delta(4) subunits in the mouse and rat retina. J Comp Neurol 521:2486–2501. CrossRef Medline

Dolphin AC (2012a) Calcium channel auxiliary $\alpha2\delta$ and β subunits: trafficking and one step beyond. Nat Rev Neurosci 13:542–555. CrossRef Medline

Dolphin AC (2012b) Calcium channel alpha2delta subunits in epilepsy and as targets for antiepileptic drugs. In: Jasper's basic mechanisms of the epilepsies, Ed 4 (Noebels JL, Avoli M, Rogawski MA, Olsen RW, Delgado-Escueta AV, eds). Bethesda, MD: National Center for Biotechnology Information.

Dolphin AC (2013) The alpha2delta subunits of voltage-gated calcium channels. Biochim Biophys Acta 1828:1541–1549. CrossRef Medline

Donato R, Page KM, Koch D, Nieto-Rostro M, Foucault I, Davies A, Wilkinson T, Rees M, Edwards FA, Dolphin AC (2006) The ducky(2J) mutation in Cacna2d2 results in reduced spontaneous Purkinje cell activity and altered gene expression. J Neurosci 26:12576–12586. CrossRef Medline

Dou H, Vazquez AE, Namkung Y, Chu H, Cardell EL, Nie L, Parson S, Shin HS, Yamoah EN (2004) Null mutation of alpha1D Ca2+ channel gene results in deafness but no vestibular defect in mice. J Assoc Res Otolaryngol 5:215–226. CrossRef Medline

Dulon D, Luo L, Zhang C, Ryan AF (1998) Expression of small-conductance calcium-activated potassium channels (SK) in outer hair cells of the rat cochlea. Eur J Neurosci 10:907–915. CrossRef Medline

Edvardson S, Oz S, Abulhijaa FA, Taher FB, Shaag A, Zenvirt S, Dascal N, Elpeleg O (2013) Early infantile epileptic encephalopathy associated with a high voltage gated calcium channelopathy. J Med Genet 50:118–123. CrossRef Medline

Engel J, Braig C, Rüttiger L, Kuhn S, Zimmermann U, Blin N, Sausbier M, Kalbacher H, Münkner S, Rohbock K, Ruth P, Winter H, Knipper M (2006) Two classes of outer hair cells along the tonotopic axis of the cochlea. Neuroscience 143:837–849. CrossRef Medline

Eroglu C, Allen NJ, Susman MW, O'Rourke NA, Park CY, Ozkan E, Chakraborty C, Mulinyawe SB, Annis DS, Huberman AD, Green EM, Lawler J, Dolmetsch R, Garcia KC, Smith SJ, Luo ZD, Rosenthal A, Mosher DF, Barres BA (2009) Gabapentin receptor alpha2delta-1 is a neuronal thrombospondin receptor responsible for excitatory CNS synaptogenesis. Cell 139:380–392. CrossRef Medline

Fuller-Bicer GA, Varadi G, Koch SE, Ishii M, Bodi I, Kadeer N, Muth JN, Mikala G, Petrashevskaya NN, Jordan MA, Zhang SP, Qin N, Flores CM, Isaacsohn I, Varadi M, Mori Y, Jones WK, Schwartz A (2009) Targeted disruption of the voltage-dependent calcium channel alpha2/delta-1-subunit. Am J Physiol Heart Circ Physiol 297:H117–H124. CrossRef Medline

Geisler S, Schöpf CL, Obermair GJ (2015) Emerging evidence for specific neuronal functions of auxiliary calcium channel $\alpha2\delta$ subunits. Gen Physiol Biophys 34:105–118. CrossRef Medline

Guinan JJ Jr (2006) Olivocochlear efferents: anatomy, physiology, function, and the measurement of efferent effects in humans. Ear Hear 27:589–607. CrossRef Medline

Hafidi A, Beurg M, Dulon D (2005) Localization and developmental expression of BK channels in mammalian cochlear hair cells. Neuroscience 130:475–484. CrossRef Medline

Hecker DJ, Lohscheller J, Bader CA, Delb W, Schick B, Dlugaiczyk J (2011) A new method to analyze distortion product otoacoustic emissions (DPOAEs) in the high-frequency range up to 18 kHz using windowed periodograms. IEEE Trans Biomed Eng 58:2369–2377. CrossRef

Hendrich J, Van Minh AT, Heblich F, Nieto-Rostro M, Watschinger K, Striessnig J, Wratten J, Davies A, Dolphin AC (2008) Pharmacological disruption of calcium channel trafficking by the alpha2delta ligand gabapentin. Proc Natl Acad Sci U S A 105:3628–3633. CrossRef Medline

Ivanov SV, Ward JM, Tessarollo L, McAreavey D, Sachdev V, Fananapazir L, Banks MK, Morris N, Djurickovic D, Devor-Henneman DE, Wei MH, Alvord GW, Gao B, Richardson JA, Minna JD, Rogawski MA, Lerman MI (2004) Cerebellar ataxia, seizures, premature death, and cardiac abnormalities in mice with targeted disruption of the Cacna2d2 gene. Am J Pathol 165:1007–1018. CrossRef Medline

Johnson SL, Marcotti W, Kros CJ (2005) Increase in efficiency and reduction in Ca2+ dependence of exocytosis during development of mouse inner hair cells. J Physiol 563:177–191. CrossRef Medline

Khimich D, Nouvian R, Pujol R, Tom Dieck S, Egner A, Gundelfinger ED, Moser T (2005) Hair cell synaptic ribbons are essential for synchronous auditory signalling. Nature 434:889–894. CrossRef Medline

Knirsch M, Brandt N, Braig C, Kuhn S, Hirt B, Münkner S, Knipper M, Engel J (2007) Persistence of $Ca_v1.3$ Ca^{2+} channels in mature outer hair cells supports outer hair cell afferent signaling. J Neurosci 27:6442–6451. CrossRef Medline

Knoflach D, Kerov V, Sartori SB, Obermair GJ, Schmuckermair C, Liu X, Sothilingam V, Garrido MG, Baker SA, Glosmann M, Schicker K, Seeliger M, Lee A, Koschak A (2013) Cav1.4 IT mouse as model for vision impairment in human congenital stationary night blindness type 2. Channels (Austin) 7:503–513. CrossRef Medline

Kros CJ, Crawford AC (1990) Potassium currents in inner hair cells isolated from the guinea-pig cochlea. J Physiol 421:263–291. CrossRef Medline

Kros CJ, Ruppersberg JP, Rüsch A (1998) Expression of a potassium current in inner hair cells during development of hearing in mice. Nature 394:281–284. CrossRef Medline

Kuhn S, Knirsch M, Rüttiger L, Kasperek S, Winter H, Freichel M, Flockerzi V, Knipper M, Engel J (2009) Ba2+ currents in inner and outer hair cells of mice lacking the voltage-dependent Ca2+ channel subunits beta3 or beta4. Channels (Austin) 3:366–376. CrossRef Medline

Kurshan PT, Oztan A, Schwarz TL (2009) Presynaptic alpha2delta-3 is required for synaptic morphogenesis independent of its Ca2+-channel functions. Nat Neurosci 12:1415–1423. CrossRef Medline

Marcotti W, Johnson SL, Holley MC, Kros CJ (2003) Developmental changes in the expression of potassium currents of embryonic, neonatal and mature mouse inner hair cells. J Physiol 548:383–400. CrossRef Medline

Matsubara A, Laake JH, Davanger S, Usami S, Ottersen OP (1996) Organization of AMPA receptor subunits at a glutamate synapse: a quantitative Immunogold analysis of hair cell synapses in the rat organ of Corti. J Neurosci 16:4457–4467. Medline

Mendus D, Sundaresan S, Grillet N, Wangsawihardja F, Leu R, Müller U, Jones SM, Mustapha M (2014) Thrombospondins 1 and 2 are important for afferent synapse formation and function in the inner ear. Eur J Neurosci 39:1256–1267. CrossRef Medline

Missler M, Zhang W, Rohlmann A, Kattenstroth G, Hammer RE, Gottmann K, Südhof TC (2003) Alpha-neurexins couple Ca2+ channels to synaptic vesicle exocytosis. Nature 423:939–948. CrossRef Medline

Mukerji S, Windsor AM, Lee DJ (2010) Auditory brainstem circuits that mediate the middle ear muscle reflex. Trends Amplif 14:170–191. CrossRef Medline

Müller M, von Hünerbein K, Hoidis S, Smolders JW (2005) A physiological place-frequency map of the cochlea in the CBA/J mouse. Hear Res 202:63–73. CrossRef Medline

Neef J, Gehrt A, Bulankina AV, Meyer AC, Riedel D, Gregg RG, Strenzke N, Moser T (2009) The Ca^{2+} channel subunit $\beta2$ regulates Ca^{2+} channel abundance and function in inner hair cells and is required for hearing. J Neurosci 29:10730–10740. CrossRef Medline

Neely GG, Hess A, Costigan M, Keene AC, Goulas S, Langeslag M, Griffin RS, Belfer I, Dai F, Smith SB, Diatchenko L, Gupta V, Xia CP, Amann S, Kreitz S, Heindl-Erdmann C, Wolz S, Ly CV, Arora S, Sarangi R, et al (2010) A genome-wide Drosophila screen for heat nociception identifies alpha2delta3 as an evolutionarily conserved pain gene. Cell 143:628–638. CrossRef Medline

Oliver D, Klöcker N, Schuck J, Baukrowitz T, Ruppersberg JP, Fakler B (2000) Gating of Ca2+-activated K+ channels controls fast inhibitory synaptic transmission at auditory outer hair cells. Neuron 26:595–601. CrossRef Medline

Opazo P, Sainlos M, Choquet D (2012) Regulation of AMPA receptor surface diffusion by PSD-95 slots. Curr Opin Neurobiol 22:453–460. CrossRef Medline

Pierce DA, Holt SR, Reeves-Daniel A (2008) A probable case of gabapentin-related reversible hearing loss in a patient with acute renal failure. Clin Ther 30:1681–1684. CrossRef Medline

Pippucci T, Parmeggiani A, Palombo F, Maresca A, Angius A, Crisponi L, Cucca F, Liguori R, Valentino ML, Seri M, Carelli V (2013) A novel null homozygous mutation confirms CACNA2D2 as a gene mutated in epileptic encephalopathy. PLoS One 8:e82154. CrossRef Medline

Pirone A, Kurt S, Zuccotti A, Rüttiger L, Pilz P, Brown DH, Franz C, Schweizer M, Rust MB, Rübsamen R, Friauf E, Knipper M, Engel J (2014) $\alpha2\delta3$ is essential for normal structure and function of auditory nerve synapses and is a novel candidate for auditory processing disorders. J Neurosci 34:434–445. CrossRef Medline

Platzer J, Engel J, Schrott-Fischer A, Stephan K, Bova S, Chen H, Zheng H, Striessnig J (2000) Congenital deafness and sinoatrial node dysfunction in mice lacking class D L-type Ca2+ channels. Cell 102:89–97. CrossRef Medline

Rodríguez-Ballesteros M, del Castillo FJ, Martín Y, Moreno-Pelayo MA, Morera C, Prieto F, Marco J, Morant A, Gallo-Terán J, Morales-Angulo C, Navas C, Trinidad G, Tapia MC, Moreno F, del Castillo I (2003) Auditory neuropathy in patients carrying mutations in the otoferlin gene (OTOF). Hum Mutat 22:451–456. CrossRef Medline

Rüttiger L, Sausbier M, Zimmermann U, Winter H, Braig C, Engel J, Knirsch M, Arntz C, Langer P, Hirt B, Müller M, Köpschall I, Pfister M, Münkner S, Rohbock K, Pfaff I, Rüsch A, Ruth P, Knipper M (2004) Deletion of the Ca2+-activated potassium (BK) alpha-subunit but not the BKbeta1-subunit leads to progressive hearing loss. Proc Natl Acad Sci U S A 101:12922–12927. CrossRef Medline

Schimmang T, Tan J, Müller M, Zimmermann U, Rohbock K, Kôpschall I, Limberger A, Minichiello L, Knipper M (2003) Lack of Bdnf and TrkB signalling in the postnatal cochlea leads to a spatial reshaping of innervation along the tonotopic axis and hearing loss. Development 130:4741–4750. CrossRef Medline

Schindelin J, Arganda-Carreras I, Frise E, Kaynig V, Longair M, Pietzsch T, Preibisch S, Rueden C, Saalfeld S, Schmid B, Tinevez JY, White DJ, Hartenstein V, Eliceiri K, Tomancak P, Cardona A (2012) Fiji: an open-source platform for biological-image analysis. Nat Methods 9:676–682. CrossRef Medline

Schlick B, Flucher BE, Obermair GJ (2010) Voltage-activated calcium channel expression profiles in mouse brain and cultured hippocampal neurons. Neuroscience 167:786–798. CrossRef Medline

Stefanini M, De Martino C, Zamboni L (1967) Fixation of ejaculated spermatozoa for electron microscopy. Nature 216:173–174. CrossRef Medline

Südhof TC (2008) Neuroligins and neurexins link synaptic function to cognitive disease. Nature 455:903–911. CrossRef Medline

Tekin M, Akcayoz D, Incesulu A (2005) A novel missense mutation in a C2 domain of OTOF results in autosomal recessive auditory neuropathy. Am J Med Genet A 138:6–10. CrossRef Medline

Tran-Van-Minh A, Dolphin AC (2010) The $\alpha2\delta$ ligand gabapentin inhibits the Rab11-dependent recycling of the calcium channel subunit $\alpha2\delta$-2. J Neurosci 30:12856–12867. CrossRef Medline

Traynelis SF, Wollmuth LP, McBain CJ, Menniti FS, Vance KM, Ogden KK, Hansen KB, Yuan H, Myers SJ, Dingledine R (2010) Glutamate receptor ion channels: structure, regulation, and function. Pharmacol Rev 62:405–496. CrossRef Medline

Vincent PF, Bouleau Y, Safieddine S, Petit C, Dulon D (2014) Exocytotic machineries of vestibular type I and cochlear ribbon synapses display similar intrinsic otoferlin-dependent Ca^{2+} sensitivity but a different coupling to Ca^{2+} channels. J Neurosci 34:10853–10869. CrossRef Medline

Wong AB, Rutherford MA, Gabrielaitis M, Pangrsic T, Göttfert F, Frank T, Michanski S, Hell S, Wolf F, Wichmann C, Moser T (2014) Developmental refinement of hair cell synapses tightens the coupling of Ca2+ influx to exocytosis. EMBO J 33:247–264. CrossRef Medline

Wycisk KA, Budde B, Feil S, Skosyrski S, Buzzi F, Neidhardt J, Glaus E, Nürnberg P, Ruether K, Berger W (2006a) Structural and functional abnormalities of retinal ribbon synapses due to Cacna2d4 mutation. Invest Ophthalmol Vis Sci 47:3523–3530. CrossRef Medline

Wycisk KA, Zeitz C, Feil S, Wittmer M, Forster U, Neidhardt J, Wissinger B, Zrenner E, Wilke R, Kohl S, Berger W (2006b) Mutation in the auxiliary calcium-channel subunit CACNA2D4 causes autosomal recessive cone dystrophy. Am J Hum Genet 79:973–977. CrossRef Medline